ORIGINAL ARTICLE

# Unlocking autofluorescence in the era of full spectrum analysis: Implications for immunophenotype discovery projects

Vanta J. Jameson[1,2,3]  |  Tina Luke[2,3]  |  Yuting Yan[2,4]  |  Angela Hind[2,3]  |
Maximilien Evrard[2]  |  Kevin Man[2]  |  Laura K. Mackay[2]  |  Axel Kallies[2]  |
Jose A. Villadangos[2,5]  |  Hamish E. G. McWilliam[2,5]  |  Alexis Perez-Gonzalez[2,3]

[1]Department of Anatomy and Physiology, The University of Melbourne, Parkville, Victoria, Australia

[2]Department of Microbiology and Immunology, The University of Melbourne, at The Peter Doherty Institute of Infection and Immunity, Parkville, Victoria, Australia

[3]Melbourne Cytometry Platform, The University of Melbourne, Parkville, Victoria, Australia

[4]School of Medicine, Tsinghua University, Beijing, China

[5]Department of Biochemistry and Pharmacology, Bio21 Molecular Science and Biotechnology Institute, The University of Melbourne, Parkville, Victoria, Australia

**Correspondence**
Alexis Perez-Gonzalez, Department of Microbiology and Immunology, The Doherty Institute for Infection and Immunity, The University of Melbourne, 792 Elizabeth Street, Melbourne, VIC 3000, Australia.
Email: alexis.gonzalez@unimelb.edu.au

## Abstract

Understanding the complex elements affecting signal resolution in cytometry is key for quality experimental design and data. In this study, we incorporate autofluorescence as a contributing factor to our understanding of resolution in cytometry and corroborate its impact in fluorescence signal detection through mathematical predictions supported by empirical evidence. Our findings illustrate the critical importance of autofluorescence extraction via full spectrum unmixing in unmasking dim signals and delineating the expression and subset distribution of low abundance markers in discovery projects. We apply our findings to the precise definition of the tissue and cellular distribution of a weakly expressed fluorescent protein that reports on a low-abundance immunological gene. Exploiting the full spectrum coverage enabled by Aurora 5L, we describe a novel approach to the isolation of pure cell subset-specific autofluorescence profiles based on high dimensionality reduction algorithms. This method can also be used to unveil differences in the autofluorescent fingerprints of tissues in homeostasis and after immunological challenges.

**KEYWORDS**
alveolar macrophages, autofluorescence, autofluorescence discovery, autofluorescence extraction, fluorochrome brightness, full spectrum unmixing, immunophenotype discovery, instrument sensitivity, label-free cytometry, signal resolution

---

Hamish E. G. McWilliam and Alexis Perez-Gonzalez co-led this study.

## 1 | INTRODUCTION

Cytometry is commonly utilized for the discovery and depiction of cellular markers of unknown abundance and distribution. Accurate representation of markers is dependent on the cytometer's ability to resolve fluorescent signals from electronic noise and other sources of background. Fluorescence resolution is expressed in a variety of equations that describe the separation between two populations based on the differences in their mean fluorescence intensities, divided by population dispersion statistics such as variance or percentile [1–3]. Concealed in this mathematical simplicity, signal resolution is a complex function of inter-linked factors broadly assigned to three main sources: the instrument, sample, and raw data processing algorithms. Signal resolution at photon detectors rely on the cytometer's ability to generate and efficiently collect fluorescence and particle-scattered photons as particles cross laser interrogation points, while simultaneously minimizing the contribution of background sources to the measured raw signal. Cytometers as photon measuring devices contrast with other light measuring technologies, by compromising laser exposure time for analytical speed. Fluorochrome excitation at the laser interrogation point typically falls below the photobleaching maximum [4] while spectral dissection leads to photon loss, further compromising collection efficiency.

Theory enabling the in-depth characterization of sensitivity and how it impacts and predicts the resolution of dim fluorescence signals, revolves around two global performance parameters [5–9]: $Q$—the instrument's overall quantum efficiency in the *translation* of fluorochromes into photoelectrons at a given detector; and $B$—the contextual background in which particle-related photons are measured, expressed in Molecules of Equivalent Soluble Fluorophore (MESF) units [10]. $Q$ and $B$ calculations are based on a fundamental limitation at the heart of every cytometry measurement. Due to the stochastic nature of the processes involved in the translation of fluorochromes into signal, there is an inverse correlation between measurement error (coefficient of variation) at a given detector and the magnitude of the signals being measured affecting parameter distributions reporting on low abundance markers and ultimately their resolution as they decrease toward background levels [11]. The resolution of dim signals is widely used in Cytometry in the operational assessment of fluorescence and instrument sensitivity, dependent as it is on $Q$ and $B$ values, both directly affected by instrument design and specifications. These global performance parameters are not the sole contributors to the successful resolution of low abundance markers. Detector gain settings [7, 12], experimental design, staining optimization and cellular autofluorescence (AF) also influence resolution outcome. Cytometry has historically relied on fluorochrome brightness to overcome

limitations in sensitivity [1]. However, variations in cytometer design and intrinsic sensitivity convey that fluorochrome brightness rankings should be defined empirically for each instrument via calculations of stain index (SI) on markers with relatively consistent, high expressions (such as CD4), after staining at optimal fluorochrome-to-cell ratios [1, 13]. In polychromatic assay design, matching rare markers to the brightest dyes is combined with the evaluation of fluorochrome "spillover spreading" (SS) matrices [14]. Careful crosschecking and selection of minimally spreading fluorochromes to preserve the resolution of rare markers are critical steps in the optimization of large fluorochrome panels [13, 15, 16].

Long known to diminish the resolution of dim signals and compromise the accurate definition of cellular phenotypes [17–21], deciphering AF from baseline noise and its accurate rendering is a reflection on the instrument's sensitivity and quantum efficiency. Often regarded as "background" affecting the delineation of negative/positive boundaries, AF also imparts information on cell viability and stress [20], disease [22] and metabolic activity [23]. While AF may hinder marker resolution in many contexts of mammalian biology, it has enabled the definition of myeloid subsets within some tissues [24] and the "label-free" identification of phytoplankton species that have unique and exceedingly bright AF fingerprints [25]. As such, the label-free measurement of AF has been incorporated into fluorescence spectroscopy [22], two-photon and fluorescence lifetime microscopy [23, 26]. As the minimum measurable fluorescent signal carried by cells, AF can be treated as an intrinsic fluorescent marker and uncoupled from the extrinsic background captured by $B$.

Strategies for AF correction or removal out of total fluorescence measurements have been explored in the past, including the development of special instruments or its compensation as a new parameter in multicolor staining using AF-correlating detectors [21, 27–29]. In recent years, with improvements in the quality of optical and electronics design and the availability of spectral cytometers (Cytek Aurora and Sony SP6800) [13, 30, 31], the development of strategies to capture and extract AF signatures from polychromatic panel measurements without compromising data or panel size has become a widely shared goal. Although the addition of AF as a new reference during unmixing calculations adds complexity to pre-defined panels due to unanticipated spectral overlap with fluorochromes tagging critical rare markers, novel post-acquisition algorithms to mathematically resolve fluorochromes in polychromatic assays [31–35] when applied to fine measurements of spectral signatures, enhance the quality of the processed data. With their paradigm shift from emission maxima and dye brightness to full spectrum signatures, leading to the improved management of spectral similarity-driven spreading [36–38], full spectral unmixing algorithms increase the chances of success by extracting

subset-specific AF from each measurement, improving the definition of rare markers and cellular phenotypes.

In this study, we revisit AF in the context of current cytometry sensitivity theory to mathematically explain its contribution to measurement precision in cytometry, its anticipated impact on signal resolution and the definition of operational fluorochrome rankings in conventional and spectral cytometers. We also demonstrate the impact of spectral unmixing and AF extraction on the resolution of fluorescence-tagged cells carrying differing AF levels, highlighting its critical importance in cellular marker and immunophenotype discovery projects. Finally, we introduce an improved discovery workflow enabling in-depth characterization and isolation of cellular subsets with unique AF spectral signatures using dimensionality reduction algorithms based on Cytek Aurora 5L raw measurements.

## 2 | THEORY

Sensitivity theory and equations enabling the calculation of $Q$ and $B$ can be used to understand the relative impact of instrument sensitivity factors and cell AF on the resolution of dim fluorescent signals (5, 6, 8). The stochasticity of the processes involved not just in the generation of all fluorescence photons at the interrogation point, but also in the successful optical collection of these photons ultimately defining a measurable signal, leads to variations in the measurement of fluorescence intensities. This photon noise can be described by Poisson statistics, with the variance of the photoelectron distribution, $SD^2$ or $\sigma^2$, equaling the statistical photoelectrons mean at each detector, $n$:

$$\sigma^2 = n. \tag{1}$$

The number of fluorescence molecules carried by each particle ($F$) contributes to the number of fluorescence photons arriving at each detector and can be linearly related to $n$ via $Q$, representing the instrument overall quantum efficiency in the translation of fluorochromes $F$ into photoelectrons $n$ ($Q = n/F$). Particle-born autofluorescence $A$ also contributes to the number of statistical photoelectrons at each detector and for the sake of simplicity it will be expressed here as fluorochrome equivalent molecules sharing with fluorescence, the same quantum efficiency $Q$. Fluorescence and AF measurements are done in the context of particle-unrelated background noise and although the contribution of this noise to signal mean values is eliminated after baseline correction, it continues to impact on the variance of the resulting signal pulses. In sensitivity theory, background $B$ is expressed as the equivalent number of fluorochrome molecules required to produce a background-equivalent contribution to the population variance and assumed to share fluorescence's $Q$ values. Thus, considering the contribution of fluorescence, AF and background, the Poisson variance in Equation (1) can be rewritten as:

$$\sigma^2 = QF + QA + QB. \tag{2}$$

While the photoelectrons mean $\mu$, exclusively dependent on AF and fluorescence derived photoelectrons after baseline correction, is given by:

$$\mu = QF + QA. \tag{3}$$

As part of the signal amplification process, photoelectron pulses generated at each cytometer detector are converted to linear channels via a gain factor $G$ (arbitrary units [a.u.]). Since variance and mean intensity values are proportionally amplified in the process, the coefficient of variation (CV) of the photoelectron distribution will match the Poisson contribution to the overall CV at each fluorescence channel. The total measured CV is additionally a function of independent factors contributing to the measurement error such as variations in fluorescence and AF intrinsic distribution and changes in illumination at the interrogation point (laser power and pointing instability), among other factors (spatial stability of optical photon collection and detection elements). Based on statistical error propagation theory, the contribution of all independent sources of variation to the total CV associated with the final measurement is given by:

$$CV^2_{total} = CV^2_{Poisson} + CV^2_{intrinsic} + CV^2_{illumination} + \ldots + CV^2_n. \tag{4}$$

Expressing $CV^2_{Poisson}$ as a function of photoelectrons variance (Equation (2)) and mean (Equation 3) values, we obtain:

$$CV^2_{total} = \frac{QF + QA + QB}{(QF + QA)^2} + \sum_{i=1}^{n-1} CV^2_i, \tag{5}$$

where $\sum_{i=1}^{n-1} CV^2_i$ represent the sum of the contributions of all independent non-Poisson factors to the total measured error. After rearrangement and simplification, Equation (5) can be further expressed as:

$$CV^2_{total} = \frac{F + A + B}{Q(F + A)^2} + \sum_{i=1}^{n-1} CV^2_i. \tag{6}$$

Alternatively, segregating $Q$ and $B$ associated components:

$$CV^2_{total} = \frac{1}{Q(F + A)} \left(1 + \frac{B}{F + A}\right) + \sum_{i=1}^{n-1} CV^2_i. \tag{7}$$

Thus, the measuring precision for particles carrying low levels of fluorescence depends not only on the number of fluorochromes being measured, the overall quantum efficiency $Q$ and background $B$ (instrument sensitivity parameters), but the levels of AF carried by the particles. As AF and fluorescence content per cell progressively exceed background ($A$ or $F >> B$), the background associated term in the $CV^2_{Poisson}$ expression $\left(1 + \frac{B}{F+A}\right) \tilde{1}$ and Equation (7) further simplifies into:

$$CV^2_{total} = \frac{1}{Q(F + A)} + \sum_{i=1}^{n-1} CV^2_i. \tag{8}$$

In populations carrying exceedingly high levels of fluorescence or AF, $\frac{1}{Q(F+A)} \tilde{0}$, and the coefficient of variation becomes altogether independent of both signal intensity ($A$ or $F$) and instrument sensitivity factors ($Q$ and $B$ values), to be exclusively based on AF and fluorescence intrinsic distributions variation, illumination consistency, and other non-Poisson sources:

$$CV_{total}^2 = \sum_{i=1}^{n-1} CV_i^2. \tag{9}$$

In other words, when measuring dim fluorescence signals carried by rare markers on highly AF cells, the dependency of measuring precision on instrument sensitivity disappears, with AF intensity and variance dominating the values of CV in both unstained and dimly positive cells.

Sensitivity theory can also be applied to the understanding of the impact of AF on signal resolution. For simplicity, we will focus on operational fluorochrome brightness defined by the stain index Equation (1), which is closely related to resolution metrics. We will consider the resolution between fluorescence-stained and unstained populations sharing consistent levels of autofluorescence $A$ (intrinsic variation ~ 0). Fluorochrome brightness, defined via the stain index SI equation is given by:

$$SI = \frac{\mu_2 - \mu_1}{2\sigma_1}, \tag{10}$$

where $\mu_1$ and $\sigma_1$ are respectively the mean and standard deviation of the label-free AF population ("unstained") and $\mu_2$ represents the mean intensity of the fluorescent population carrying the same levels of AF. Assuming no contribution from non-Poisson sources to the measured signal error, both the variance of the negative population and the means of the positive and negative populations will be linearly related via the gain factor $G$ to the number of photoelectrons at the fluorescence detector. By using Equations (2), (3) incorporating the gain factor $G$ in the conversion of photoelectrons to channel values, Equation (10) can be rewritten as:

$$SI = \frac{G(QF + QA) - G(QA)}{2G\sqrt{QA + QB}}. \tag{11}$$

That after rearrangement and simplification, becomes:

$$SI = \frac{F}{2} \times \sqrt{\frac{Q}{(A+B)}}. \tag{12}$$

Equation (12) provides a simple relationship for SI based on values of fluorescence, carrier AF and global sensitivity parameters ($Q$ and $B$) right at the onset of the signals (photoelectron statistics-dominated CVs) and illustrates the negative impact of both measurement background and carrier AF on dim signal resolution via their contribution to the variance of the negative population. The negative effect of AF on signal resolution is further accentuated when considering the typical variation in AF intrinsic distributions observed in most biological samples.

Three relevant scenarios where the dependency of SI on carrier particle AF could lead to experimental inconsistencies are the definition of operational fluorochrome brightness ranking as a tool for panel design, the discovery of the cellular distribution and expression levels of dim fluorescent protein gene-reporters, and longitudinal studies performed on cells undergoing changes in AF intensity and signature. Let us consider the ratio between fluorescence SI calculated on cells with AF $A_1$ and $A_2$. Assuming in both cases a negligible contribution of non-Poisson sources of variation, a perfect match in fluorochrome numbers $F$ per cell and the use of the same instrument and detector and so consistent quantum efficiency $Q$ and background $B$ values, the SI ratio is given by:

$$\frac{SI_1}{SI_2} = \frac{\frac{F}{2} \times \sqrt{\frac{Q}{(A_1+B)}}}{\frac{F}{2} \times \sqrt{\frac{Q}{(A_2+B)}}}. \tag{13}$$

That becomes, after rearrangement and simplification:

$$\frac{SI_1}{SI_2} = \sqrt{\frac{(A_2 + B)}{(A_1 + B)}}. \tag{14}$$

Assuming values of $B$ are negligible, compared to $A_1$ and $A_2$ values:

$$\frac{SI_1}{SI_2} \sqrt{\frac{\tilde{A_2}}{A_1}}. \tag{15}$$

Or,

$$\frac{SI_1}{SI_2} \frac{\tilde{1}}{\sqrt{\frac{A_1}{A_2}}}. \tag{16}$$

Essentially, based on Equations (14) and (16), the ratio between SI across two populations with distinct levels of AF will be inversely proportional to the square root of the ratio of their AF values. Consequently, empirical estimations of fluor brightness rankings and their extrapolation across cellular subsets, the percentage of expression of dim fluorescent reporters across cellular subsets, and the evaluation of phenotypes including low abundance (tertiary) markers in longitudinal studies involving major immunological events (inflammation, infection) leading to drastic changes in cell activation and metabolic status will all be affected by changes in cellular AF, due to its negative effect on signal resolution and subsequently the operational brightness of fluorochromes and the accurate estimation of subset frequencies.

# 3 | MATERIAL AND METHODS

## 3.1 | Human blood processing and antibody staining for flow cytometry

Heparinized fresh human peripheral blood from healthy volunteers (University of Melbourne Human Research and Ethics Committee

2021–20,314–18,913-6) and stabilized (fixed) human blood, IMMUNO-TROL (cat #6607077, Beckman Coulter, Brea, CA, USA) were used to define the brightness of 26 unique fluorochromes conjugated to CD4 antibody (clone SK3; BD Horizon evaluation kit cat #566352, Becton Dickinson, Franklin Lakes, NJ, USA). Whole blood antibody staining was performed as per manufacturer's instructions using OptiLyse B Lysing Solution (cat #IM1400, Beckman Coulter). Briefly, leukocyte counts were performed for fresh and fixed blood samples and equivalent numbers of leukocytes within 95–105 μl of whole blood were incubated in the presence of 2 μl of antibodies for 20 min in the dark. Erythrocytes were lysed with the addition of 100 μl OptiLyse to each tube, vortexed and incubated at room temperature (RT) for 10 min. To this 1 ml of deionized water was added, vortexed and incubated for 10 min at RT. Cell preparations were spun for 3 min at 400 $\times g$ (4°C) and washed three times with 3 ml PBS/ 2% fetal calf serum (FACS wash). After washing, leukocytes pellets were resuspended in 300–500 μl of FACS wash and stored refrigerated in the dark before flow cytometric analysis.

## 3.2 | Flow cytometry and analysis

In all cases, manufacturer quality control programs were run and passed before acquisition of data. Between 5000 and 10,000 gated lymphocytes were acquired at low differential pressure (10–12 μl min$^{-1}$) on all available detectors on a CytoFLEX LX/ CytExpert software (6 laser: UV3-V5-B3-YG5-R3-IR2, Beckman Coulter) and an Aurora 5L/SpectroFlo® software (5 laser: UV16-V16-B14-YG10-R8, Cytek, Fremont, CA, USA).

Raw FCS data files were used to calculate SI from both CytoFLEX and Aurora cytometers. Additionally, for Aurora, each fluorochrome was unmixed independently with and without AF extraction using unstained lymphocytes as a reference for AF via SpectroFlo. Henceforth, unmixed, AF extracted data is referred to as (U-AF) and unmixed, no AF extraction is referred to as (U). CD4$^+$ SI were calculated based on the mean fluorescence intensity (MFI) for both CD4$^+$ and CD4$^-$ lymphocytes and the standard deviation (SD) of CD4$^-$, based on Equation (10):

Normalized stain index (SI$_{norm}$) at each detector was additionally calculated based on calculated SI per detector and maximum stain index value across all detectors for each fluorochrome (SI$_{max}$), based on this equation:

$$SI_{norm} = \frac{SI}{SI_{max}}. \tag{17}$$

## 3.3 | Fluorescent tdTomato reporter mice

The tdTomato (Tom+/+) reporter mice were generated by inserting the tdTomato sequence in frame following the promotor region of a gene with weak expression. This was performed by the MAGEC laboratory as previously reported (39), complying with relevant ethical regulations and approved by the Walter and Eliza Hall Institute (WEHI) Animal Ethics Committee. Briefly, 20 ng/μl$^{-1}$ of Cas9 mRNA, 10 ng/μl$^{-1}$ of sgRNA (targeting the insertion site) and 6 ng/μl$^{-1}$ of the targeting vector (containing the tdTomato coding sequence and flanked by homology arms) were injected into the pronucleus of fertilized one-cell stage embryos generated from wild-type C57BL/6J breeders. Twenty-four hours later, two-cell stage embryos were transferred into the uteri of pseudo-pregnant female mice. Targeted animals were backcrossed to wild-type C57BL/6J mice.

C57BL/6 (WT) and Tom+/+ mice were bred and maintained in specific pathogen–free conditions at the Bio21 Molecular Science and Biotechnology Institute. Experiments were performed on 9–11 weeks old mice in accordance with the Institutional Animal Care and Use Committee guidelines of the University of Melbourne.

## 3.4 | Murine infection and fasting models

All animal experiments were approved by the University of Melbourne Animal Ethics Committee.

C57BL/6 (C57BL/6JArc) mice used in the infection model were purchased from the Animal Resource Centre (Murdoch, WA, Australia) and maintained in specific pathogen–free conditions in the Department of Microbiology and Immunology at the University of Melbourne. Female mice were used for experiments at 6–12 weeks of age. LCMV infection was performed by intraperitoneal injection of $2 \times 10^5$ pfu of the Armstrong strain (acute strain) or by intravenous injection of $2 \times 10^6$ pfu of the CL13 strain (chronic strain). Organs were harvested 30 days after LCMV infection.

C57BL/6J used in the fasting model were bred and maintained in specific pathogen–free conditions at the Peter Doherty Institute of Infection and Immunity. Analysis was undertaken with mice aged 9–11 weeks old. Every other day fasting (EODF) was performed on male C57BL/6J mice starting at 8 weeks of age for 2 months and housed under standard vivarium conditions (22°C). Mice were randomly grouped to ad libitum (AL) or every other day fasting (EODF) group, while fed standard chow diet. The AL group was allowed unrestricted access to food, while the EODF group was fed with alternating 24 h periods of free access to food followed by 24 h of fasting (40).

## 3.5 | Murine tissue processing and antibody staining for flow cytometry

In all cases, mice were euthanized using $CO_2$ and then perfused with 10 ml PBS injected into the right ventricle of the heart. Lungs were harvested and finely diced with a scalpel blade and then digested with Liberase (0.25 mg/ml; Roche)/DNase I (5 μg/ml; Roche) in Hank's balanced salt solution (HBSS) for 60 min at 37°C. After vigorous mixing with a 1 ml pipette tip, the cells were passed through 70 μm mesh. Skin cells were isolated as previously described (41). Briefly, shaved, and depilated skin from the mouse flank (3 cm$^2$) was removed and

**TABLE 1** Flow cytometry staining panel for defining lung and spleen cells

| Antibody | Fluorochrome | Clone | Company | Catalogue # |
| --- | --- | --- | --- | --- |
| Ly6G | BUV395 | 1A8 | BD Biosciences | 583778 |
| TCRβ | BUV805 | H57-597 | BD Biosciences | 748405 |
| MerTK | BV421 | 2B10C42 | Biolegend | 151510 |
| CD11b | BV510 | M1/70 | Biolegend | 101263 |
| SiglecF | BV650 | E50-2440 | BD Biosciences | E50-2440 |
| CD45 | BV786 | 30-F11 | BD Biosciences | 56425 |
| CD11c | FITC | N418 | WEHI | N/A |
| CD19 | BB700 | 1D3 | BD Biosciences | 566411 |
| CD64 | APC | X54-5/7.1 | Biolegend | 139306 |
| MHC-II | AF700 | M5/114.15.2 | Biolegend | 107622 |
| Fixable viability dye | eFluor780 | N/A | ThermoFisher | 65-0865-14 |

incubated in Dispase solution (2.5 mg/ml; Roche) for 90 min at 37°C. Epidermal and dermal layers were separated, then diced, combined and placed in collagenase III solution (3 mg/ml; Worthington) containing DNase I (2.5 μg/ml) and incubated for a further 30 min at 37°C. Spleens were forced through 70 μm mesh without digestion. Cells were centrifuged (800×g, 7 min, 4°C). Livers were forced through 70 μm mesh and pellets were resuspended in 35% isotonic Percoll (GE Healthcare) prior to density gradient centrifugation (500×g, 20 min). Spleen and liver red blood cells were lysed using 1X RBC lysis buffer (eBioscience). Kidneys and salivary glands placed in Collagenase III (3 mg/ml; Worthington) and DNAse I (5 μg/ml; Roche), chopped into fine pieces and further incubated for 30 min at 37°C. Digested pieces were homogenized, passed through a 70 μm strainer, and lymphocytes were purified using a 44/70% Percoll gradient centrifugation. For isolation of visceral adipose tissue (VAT) immune cells, perigonadal VAT was isolated, finely minced and suspended in 0.025% collagenase type IV (Gibco) (2 ml collagenase per gram fat). The suspension was incubated for 45 min at 37°C in a shaker. After incubation, the suspension was 10 times diluted with phosphate buffered solution (PBS) + 2% FCS and centrifuged at 800×g for 15 min at 4°C. The upper adipocyte fraction was discarded and the stromal vascular fraction that pelleted was resuspended in red blood cell lysis buffer (ACK RBC Lysis Buffer). Recovered cells were washed and strained through a 70 μm mesh (42).

Cell preparations from all organs were resuspended in FACS wash and analyzed without labelling with antibodies. For tdTomato expression studies, WT and Tom+/+ spleen and lung samples were also incubated with Fc blocking reagent (anti-CD16/CD32, clone 2.4G2, WEHI, 40 μg/mL), and then stained with antibody panels as described in Table 1. Antibody-labeled and unlabeled counterparts were acquired using CytoFLEX LX and Aurora 5L cytometers.

## 3.6 | Data processing and high dimensional analysis of autofluorescence

Aurora 5L raw FCS files containing WT or Tom unstained mouse lung, spleen and skin cells were collected and stored in the online analysis platform OMIQ (CBInsights). Off-scale and debris events were excluded from analysis by scatter gating before performing analysis on non-debris, non-erythrocyte singlet populations. Default OMIQ fluorescence parameter scaling was applied (type = arcsinh[$x/c$], cofactor = 6000) followed by subsampling of gated events to include $3 \times 10^5$ cells from each lung and spleen WT unstained replicas and all available skin gated events (3.7–$4.8 \times 10^4$ per WT replica file). Opt-SNE for a combined total of $1.9 \times 10^6$ events was run based on all raw fluorescence parameters (64), using the following OMIQ settings: maximum iterations = 1000, opt-SNE End = 5000, Perplexity = 30, Theta = 0.5, components = 2, Verbosity = 25 and random seed values. OMIQ was also used for the manual gating of opt-SNE AF populations, the generation of data files containing MFI statistics across all detectors for Prism 9 (GraphPad) analysis of spectral correlations via Pearson r and the generation FCS files from gated opt-SNE AF populations for further analysis. Similar workflows were run with FlowJo (version 10, Becton Dickinson) and FCS Express (version 7, De Novo Software). Raw FCS files from unstained lung, spleen and skin Aurora 5L samples from one WT (Tom −/−) mouse were analyzed in Flowjo. Gated singlets from each tissue (50,000 cells) were concatenated and analyzed with opt-SNE based on all fluorescence parameters (64), using the following Flowjo settings: iterations = 1000, learning rate (eta) = 10,500, Perplexity = 30, KNN algorithm = Exact (vantage point tree), gradient algorithm = Barnes-Hut. In FCS Express, concatenated gated singlets (interval downsampling of 50,000 events) from unstained spleen, lung, and skin from three WT (Tom −/−) mice were analyzed with opt-SNE based on all fluorescence parameters (64), using the following algorithm settings: iterations = 500, method = Barnes-Hut, Amount of approximation = 0.50, Perplexity = 30, random seed.

## 4 | RESULTS

### 4.1 | Autofluorescence influences fluorochrome brightness rankings in conventional and spectral cytometers

To aid immunophenotyping panel design for complex biological samples, brightness rankings (stain index; SI) of commonly used
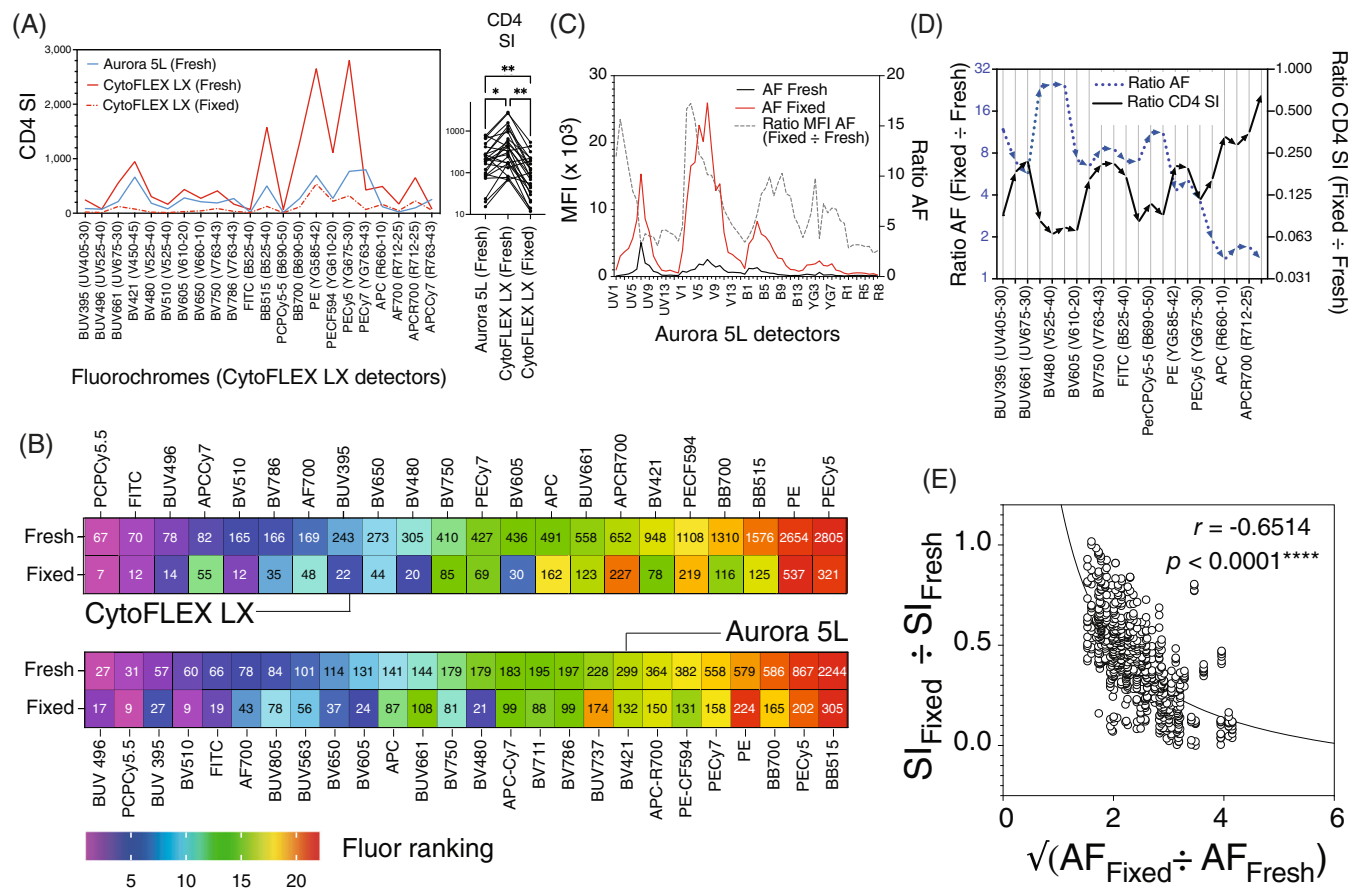
**FIGURE 1** Fluorescence resolution depends on instrument sensitivity and carrier AF. (A) Comparison of CD4+ lymphocyte SI across 22 fluorochromes for fresh and fixed blood on CytoFLEX LX (gains = 500, raw data) and Aurora 5L (CAS, U data). Compared to CytoFLEX fresh, SI are significantly (ANOVA multiple comparisons) reduced on fixed (**$p < 0.01$) and Aurora fresh samples (*$p < 0.05$). (B) Fluorochrome brightness ranking (stain index, SI) changes between fresh and fixed calculated at Aurora and CytoFLEX primary detectors. (C) MFI and ratio of fixed and fresh unstained lymphocytes across Aurora 5L 64 detectors demonstrate enhanced autofluorescence (AF) across violet, UV and blue laser detectors in fixed. (D) Inverse relationship between dye brightness and carrier AF illustrated via opposite trends in AF and fluorochrome SI ratio (fixed: fresh cells) at expected maxima emission detectors in CytoFLEX. (E) There is a significant ($p < 0.0001$) inverse correlation between SI and AF ratios (Pearson $r - 0.6514$). SI for each fluorochrome was calculated from raw data across 64 Aurora detectors. Detectors were included in calculations only when $SI_{fresh} > 1.0$ (total 729). Ratio ($SI_{fixed}/SI_{fresh}$) plotted against mean AF ratio values ($AF_{fixed}/AF_{fresh}$) at matching detectors [Color figure can be viewed at wileyonlinelibrary.com]

fluorochromes (representing UV-red excitation and violet-IR emission) were defined on fresh human blood. CD4+ lymphocytes were labeled and samples analyzed on both Aurora 5L (at Cytek recommended assay settings [CAS] following QC) and CytoFLEX LX (at avalanche photodiode detectors gain = 500, where max dim signal resolution was reached for most fluorescence detectors, see Figure S1). Fluorochrome brightness in the CytoFLEX was measured at each respective primary (maximum fluorescence emission) detector and based on raw (uncompensated) data, while Aurora brightness calculations were based on spectrally unmixed fluorescence parameters with SpectroFlo. Except where sub-optimal bandpass filters (763/43 nm) for far-red detection are installed in the CytoFLEX LX to circumvent 808 nm laser noise into far-red emission detectors, SI across all fluorochromes in the CytoFLEX were found to be consistently higher than in Aurora (Figure 1A). The superior sensitivity of the CytoFLEX was expected as previously observed when comparing SI of Rainbow 8-peaks calibration particles (Spherotech) run at Aurora CAS settings

or after CytoFLEX APD gain titration where CytoFLEX outperformed Aurora even at suboptimal gains (Figure S1).

We then evaluated the effect of AF on SI and fluorochrome brightness ranking, by comparing CytoFLEX fresh blood results with Immunotrol, a liquid preparation of stabilized (henceforth depicted as "fixed") whole human blood stained with the same fluorochromes. We observed a significant reduction in SI for all fluorochromes in fixed compared to fresh samples (Figure 1A). Interestingly, apart from the brightest-ranked (PE and PE-Cy5) and dimmest-ranked (FITC and PerCP-Cy5.5) fluorochromes, in both fresh and fixed samples, most fluorochromes were re-ranked in their brightness scale when applied to fixed samples (Figure 1B). Notably, red to infrared-emitting fluorochromes (such as BV786, APC, Alexa Fluor 700 and APC-Cy7) increased their brightness rankings in fixed samples, whereas blue to yellow emitting dyes' rankings decreased (such as BUV496, BV510, BV421, BV605, and BB515). These blue to yellow emitting fluorochromes re-ranked as dimmer on fixed cells have peak emissions at or close to the maximum emission of AF

~525 nm (Figures 1C and S2A,B). Additionally, fixed normalized CD4 SI, when viewed across all CytoFLEX detectors, revealed changes in resolution patterns for most fluorochromes away from their predicted fluorescence emission patterns when compared to fresh cells (Figure S3A). These changes in SI in non-primary (or spillover) channels, relative to the primary resolution channel correlated inversely with AF ratio and was best appreciated in dyes with complex excitation and emission properties such as PerCP-Cy5.5 (Ex$_{max}$ = 482 nm, Em$_{max}$ = 695 nm) and BB700 (Ex$_{max}$ = 476 nm, Em$_{max}$ = 695 nm). Both showed complete inversions in normalized SI patterns leading to maximum resolution at the R712/25 detector in fixed samples, instead of their expected primary B690/50 detector (Figure S3B). The opposing trends of increasing AF and decreasing SI ratios for fluorochromes at their primary detectors is illustrated in Figure 1D and is supported by a significant negative correlation (Pearson $r = -0.6261$, $p < 0.001$) between AF and signal resolution when considering AF and SI ratios for each fluorochrome across primary and spillover detectors where SI$_{fresh}$ >1.0 (Figure S2C) as predicted by Equation (16).

We expanded the analysis of the correlation between dye brightness and cell AF to Aurora 5L. The results confirmed the differences in AF levels between the fixed and fresh samples, provided fine details on the AF signatures of unstained fresh and fixed lymphocytes (Figure 1C), and the spectral similarity of unstained fixed sample AF to BV480 and BV510 and fresh AF to BUV496 (Figure S4). In all cases, fluorochromes on fixed lymphocytes had lower SI than their fresh counterparts (raw data SI, Figure S5). To evaluate the correlation between SI and AF ratios, fixed and fresh CD4 SI were calculated for each fluorochrome based on raw data files across all 64 Aurora detectors. As for CytoFLEX, fixed and fresh SI data pairs for each detector (where SI fresh >1.0 [total 729]) were selected and their ratio (SI$_{fixed}$/SI$_{fresh}$) evaluated against mean AF ratio values (AF$_{fixed}$/AF$_{fresh}$) at matching detectors. As expected, a significant inverse correlation between SI and AF ratios was observed (Figure 1E). Due to their fundamental optical differences, Aurora and CytoFLEX fluorochrome brightness rankings differed (Figure 1B). Notwithstanding, brightness ranking and normalized SI across detectors in both instruments was impacted by the intensity of AF spectral signatures (Figures S3 and S6).
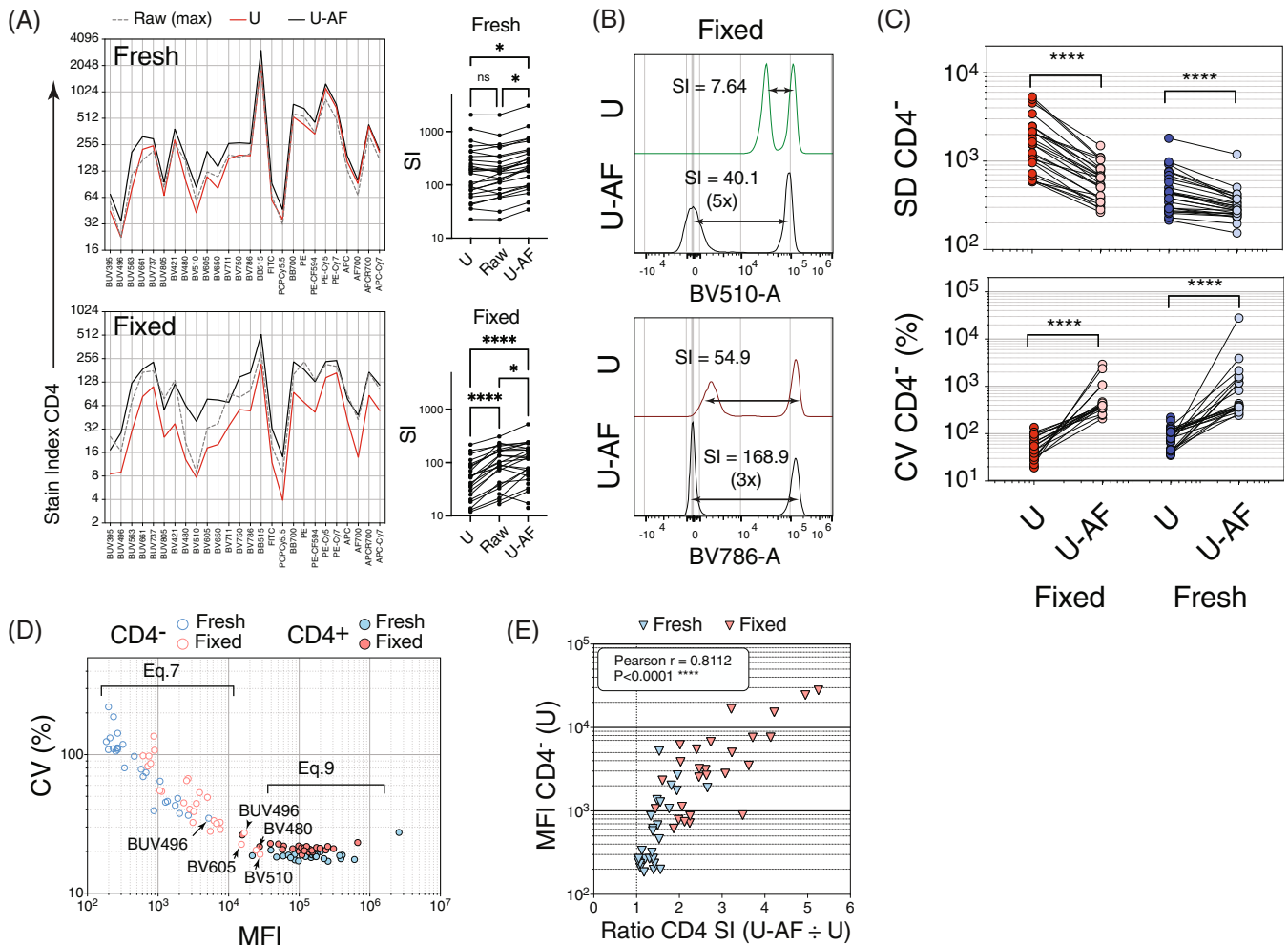
While we controlled the ratio of antibody to cells by matching fresh and fixed leukocyte numbers before staining, we needed to exclude the possibility that the reduction in SI in fixed samples was due to a reduction in available CD4 epitopes or variations in antibody to CD4 ratios. Overall, we found roughly even MFI values for CD4$^+$ events for fluorochromes staining fresh or fixed samples (Figures S7 and S8A). It was the increase in AF intensity, the reduction in the ratio of positive and negative population MFI and the high variance in CD4- lymphocytes in fixed samples that lead to a dramatically decreased SI of fluorochromes in fixed samples (Figure S8B). Finally, changes in the normalized SI across Aurora detectors were not due to "particle carrier effects" where fluorochrome emission may be altered (due to Förster resonance energy transfer [FRET] or other interference) dependent on the type of particle to which they are bound. We observed an almost perfect match in data-derived normalized fluorescence spectra between fixed and fresh samples when viewed across all Aurora detectors (Figure S9).

## 4.2 | Full spectrum unmixing and autofluorescence extraction impact on resolution

Given the significant negative impact of increased AF on the resolution of fluorochromes with emission close to high AF regions, we next evaluated what improvement full spectrum unmixing and AF extraction could provide to fluorochrome brightness and signal resolution using stained fresh and fixed lymphocytes. Some of the fluorochromes evaluated in our study share similar emission spectra based on Fluorochrome Similarity™ Index (a metric developed by Cytek used to compare spectral signatures and based on the cosine of the angle between vectors defined for each fluorochrome in a 64-dimensional space, (13)). For instance, BB515/FITC and APC-R700/Alexa Fluor 700 pairs have Similarity™ Indices of 0.98 and 0.96, respectively (https://spectrum.cytekbio.com/). To minimize spreading errors affecting the calculations of SI and resulting from the unmixing of fluorochromes with close emission spectra, fluorochromes were unmixed one at a time with SpectroFlo. SI for 26 dyes was calculated based on raw data (maximum SI across 64 detectors), after spectral unmixing (U) and unmixing with AF extraction (U-AF) (Figure 2A). While in fresh samples U alone did not improve SI over raw data, U-AF marginally improved CD4 SI over both raw and U values. Contrasting with fresh results, U in fixed lymphocytes lead to significantly worse resolution compared to raw data. Conversely, U-AF significantly improved CD4 SI over U values, and SI above raw levels for most fluorochromes, especially for those with emission maximum in spectral regions where AF also reaches maximum values. For example, while positive MFI were only marginally affected (if at all), removing the AF contribution from fluorochromes impacted by high AF (BV510) lead to an increased dynamic range (SI), by decreasing the MFI of the negative populations (Figure 2B). SI improvement was also seen but was less dramatic for fluorochromes less impacted by AF (BV786). This decrease in CD4$^-$ intensity following U-AF (compared to U only) is demonstrated for all fluorophores tested (Figure S10).

While U-AF improved dynamic range over raw and U measurements, by decreasing the MFI of negative populations, this generated more spreading around the negatives, increasing their $CV$ (Figure 2C). As such, understanding when to apply U-AF is knowing how to balance 2 opposing effects: the resolution gain from decreasing the MFI of the negative populations and the resolution reduction from the increase in the spreading error of this process. If U-AF is applied to cases of low AF MFI, this spreading artifact could overshadow the gain from dynamic range increase and be detrimental to the resolution of dim markers. To predict U-AF-derived benefits to resolution over U results, we evaluated the correlation between SI ratio (SI$_{U-AF}$/SI$_U$) and MFI values of negative populations after unmixing without AF extraction (U). Despite the differences in APD gain per detector in Aurora at Cytek Assay settings, the MFI values for the negative populations after unmixing (U) can be used as indicators of absolute AF content. A correlation between the $CV$ and MFI of negative populations after unmixing without AF extraction (U) was observed (Figure 2D), similar to the relationship between $CV$ and signal intensity illustrated by Equation (7). Fluorochromes including BV510, BV480, and BV605,

ISAC
INTERNATIONAL SOCIETY FOR
ADVANCEMENT OF CYTOMETRY
CYTOMETRY
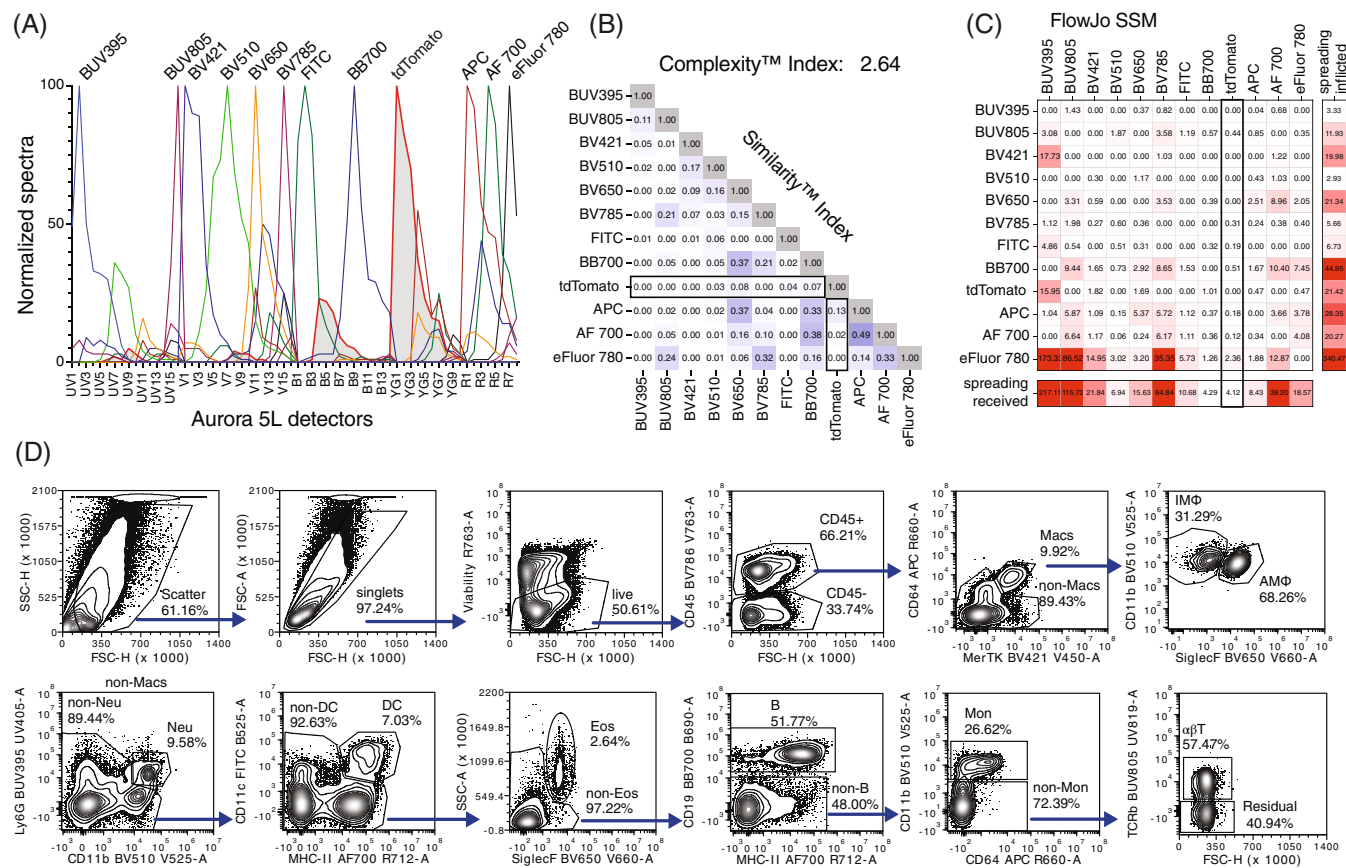Journal of Quantitative Cell Science PART A



**FIGURE 2** Stain index (SI) of fluorochromes emitting in spectral regions of high autofluorescence (AF) is improved after full spectral unmixing with autofluorescence extraction (U-AF). (A) SI of 26 fluorochromes bound to CD4 lymphocytes in fresh or fixed samples run on Aurora showing raw, unmixed (U) and U-AF comparisons. Note the significantly ($p < 0.0001$) improved resolution of U-AF SI compared to raw and U in fixed compared to marginal ($p < 0.05$) improvements in fresh. (B) Examples of the effect of U-AF versus U on SI in fixed samples. Note the increase in CD4+/CD4− separation in fluorochromes emitting in regions of high AF (BV510) versus low AF (BV786). (C) CD4− standard deviation (SD) and coefficient of variation (CV) in fixed and fresh after U or U-AF demonstrate significant global differences ($p < 0.0001$) and the increase in measurement spread after U-AF. (D) CV versus MFI of CD4− and CD4+ populations in fixed and fresh. CD4− cells from fixed samples detected in regions of high AF have high relative MFI and reduced CVs approaching that of CD4+ cells, illustrating the effect of high AF on measurement precision as per Equation (7). (E) The MFI of CD4− populations after U correlates with SI improvement after AF extraction (U-AF). In Aurora this can be used to predict the gain in SI after AF extraction. For example, negative population MFI $\sim 10^4$ after U can anticipate 4–5× increase of SI after U-AF whereas negative U MFI $< 10^3$ will expect only a marginal SI improvement with AF extraction (1–2×) [Color figure can be viewed at wileyonlinelibrary.com]

with negative (AF) populations with MFI $\sim 10^4$ and with low CV, as an indirect measure of AF intensity (CV $\sim$ 20% in CD4+ cells, minimum values with negligible Poisson contribution), will benefit most from U-AF. This was confirmed after evaluating CD4 SI improvement (SI$_{U-AF}$/SI$_U$) against unmixed negative population MFI (Figure 2E). The SI of fluorochromes with unmixed CD4− MFI values $\sim$2x10$^2$, (CV > 80%), does not improve after AF extraction, while the SI of fluorochromes with high AF MFI values around 10$^4$ (U) increases $\sim$4-fold after U-AF. These findings have significant implications for studies of cellular subsets in complex tissues, allowing us to predict when to apply U-AF to accurately define dim marker expression.

## 4.3 | Panel design and analysis strategies to characterize dim signals in highly AF samples

We applied our understanding of the impact of increasing AF on signal resolution to a biologically relevant setting: the assessment of the cellular expression and tissue distribution of a tdTomato (Tom) fluorescent protein reporting on the expression of a weakly expressed gene involved in the immune system in homozygous Tom+/+ mice. Antibody panels were designed to assess the expression of Tom across several tissues, including lungs, and broadly targeting several hematopoietic subsets: B and αβT lymphocytes, eosinophils, dendritic cells,

**(A)** Normalized spectra — Aurora 5L detectors (fluorochromes: BUV395, BUV805, BV421, BV510, BV650, BV785, FITC, BB700, tdTomato, APC, AF 700, eFluor 780)

**(B)** Complexity™ Index: 2.64 — Similarity™ Index matrix

| | BUV395 | BUV805 | BV421 | BV510 | BV650 | BV785 | FITC | BB700 | tdTomato | APC | AF 700 | eFluor 780 |
|---|---|---|---|---|---|---|---|---|---|---|---|---|
| BUV395 | 1.00 | | | | | | | | | | | |
| BUV805 | 0.11 | 1.00 | | | | | | | | | | |
| BV421 | 0.05 | 0.01 | 1.00 | | | | | | | | | |
| BV510 | 0.02 | 0.00 | 0.17 | 1.00 | | | | | | | | |
| BV650 | 0.02 | 0.00 | 0.09 | 0.16 | 1.00 | | | | | | | |
| BV785 | 0.00 | 0.21 | 0.07 | 0.03 | 0.15 | 1.00 | | | | | | |
| FITC | 0.01 | 0.00 | 0.01 | 0.06 | 0.00 | 0.00 | 1.00 | | | | | |
| BB700 | 0.00 | 0.05 | 0.00 | 0.05 | 0.37 | 0.21 | 0.02 | 1.00 | | | | |
| tdTomato | 0.00 | 0.00 | 0.00 | 0.03 | 0.08 | 0.00 | 0.00 | 0.07 | 1.00 | | | |
| APC | 0.00 | 0.02 | 0.00 | 0.02 | 0.37 | 0.04 | 0.00 | 0.33 | 0.13 | 1.00 | | |
| AF 700 | 0.00 | 0.05 | 0.00 | 0.01 | 0.16 | 0.10 | 0.00 | 0.38 | 0.02 | 0.49 | 1.00 | |
| eFluor 780 | 0.00 | 0.24 | 0.00 | 0.01 | 0.06 | 0.32 | 0.00 | 0.16 | 0.00 | 0.14 | 0.33 | 1.00 |

**(C)** FlowJo SSM

| | BUV395 | BUV805 | BV421 | BV510 | BV650 | BV785 | FITC | BB700 | tdTomato | APC | AF 700 | eFluor 780 | spreading inflicted |
|---|---|---|---|---|---|---|---|---|---|---|---|---|---|
| BUV395 | 0.00 | 1.43 | 0.00 | 0.00 | 0.37 | 0.82 | 0.00 | 0.00 | 0.00 | 0.04 | 0.68 | 0.00 | 3.33 |
| BUV805 | 3.08 | 0.00 | 0.00 | 1.87 | 0.00 | 3.58 | 1.19 | 0.57 | 0.00 | 0.44 | 0.85 | 0.35 | 11.93 |
| BV421 | 17.73 | 0.00 | 0.00 | 0.00 | 1.03 | 0.00 | 0.00 | 0.00 | 0.00 | 0.00 | 1.22 | 0.00 | 19.98 |
| BV510 | 0.00 | 0.00 | 0.30 | 0.00 | 1.17 | 0.00 | 0.00 | 0.00 | 0.00 | 0.43 | 1.03 | 0.00 | 2.93 |
| BV650 | 0.00 | 3.31 | 0.59 | 0.00 | 0.00 | 3.53 | 0.00 | 0.00 | 0.00 | 2.51 | 8.96 | 2.05 | 21.34 |
| BV785 | 1.12 | 1.98 | 0.27 | 0.60 | 0.36 | 0.00 | 0.00 | 0.00 | 0.00 | 0.24 | 0.38 | 0.40 | 5.66 |
| FITC | 4.86 | 0.54 | 0.00 | 0.51 | 0.24 | 0.00 | 0.00 | 0.00 | 0.00 | 0.32 | 0.19 | 0.00 | 6.73 |
| BB700 | 0.00 | 9.44 | 1.65 | 0.73 | 2.92 | 8.65 | 1.53 | 0.00 | 0.00 | 0.51 | 10.40 | 7.45 | 44.95 |
| tdTomato | 15.95 | 0.00 | 1.82 | 0.00 | 1.69 | 0.00 | 0.00 | 1.01 | 0.00 | 0.47 | 0.00 | 0.47 | 21.42 |
| APC | 1.04 | 5.87 | 1.09 | 0.15 | 5.37 | 5.72 | 1.12 | 0.37 | 0.18 | 0.00 | 3.66 | 3.78 | 28.35 |
| AF 700 | 0.00 | 6.64 | 1.17 | 0.06 | 2.24 | 6.17 | 1.11 | 0.36 | 0.12 | 0.34 | 0.00 | 4.08 | 20.27 |
| eFluor 780 | 173.3 | 86.52 | 14.95 | 3.02 | 3.20 | 35.35 | 5.73 | 1.26 | 2.36 | 1.88 | 12.87 | 0.00 | 340.47 |
| spreading received | 217.11 | 115.71 | 21.84 | 6.94 | 15.63 | 64.64 | 10.68 | 4.29 | 4.12 | 8.43 | 39.20 | 18.57 | |

**(D)** Gating strategy

FIGURE 3 Designing lung panel and gating strategy for Tom reporter discovery by spectral and conventional cytometers. (A) Normalized spectra of fluorochromes for a lung panel chosen to avoid tdTomato spectral overlap. Spectral visualization was based on FCS Express OLS unmixing matrix values, calculated with single color reference controls acquired in Aurora 5L. (B) Similarity™ index matrix of lung panel fluorochromes using Cytek full Spectrum viewer based on Aurora 5L (16UV-16V-14B-10YG-8R) configuration (https://spectrum.cytekbio.com/). Note the very low panel Complexity™ index (2.64) and negligible similarity of chosen fluorochromes to tdTomato. (C) Flowjo spillover spreading (SS) matrix based on single color controls acquired in CytoFLEX LX, confirming the minimal spreading received at the tdTomato channel (Y585/42 detector). (D) Gating strategy used to identify main subsets in lung samples acquired in CytoFLEX LX and Aurora 5L. Hierarchical gating relationships across plots are represented by arrows. CD45− cells and CD45+ leukocytes were defined after doublets and dead cells were excluded. Within the CD45+ cells, macrophages (Macs) were identified as MerTK+CD64+ and further analyzed in terms of SiglecF and CD11b expression for the identification of lung resident alveolar (AMΦ) and interstitial (IMΦ) macrophages. Out of the remaining CD45+ cells (non-Macs), neutrophils (Neu) were gated based on expression of CD11b and Ly6G and the remaining cells progressively analyzed for the identification of dendritic cells (DC, MHC-II+ CD11c+), eosinophils (Eos, SiglecF+ SSChi), B lymphocytes (CD19+), monocytes (Mon, CD11b+ CD64lo), αβT lymphocytes (TCRβ+) and CD45+ residual cells (negative for all cell surface markers except CD45) [Color figure can be viewed at wileyonlinelibrary.com]

neutrophils, monocytes, lung interstitial macrophages (IMΦ) and alveolar macrophages (AMΦ). Based on previous observations and extrapolated biological function of the immune marker, Tom expression was predicted to be very low. We were therefore interested in comparing the CytoFLEX LX with exquisite sensitivity in the primary Tom channel YG585/42 (Figures 1A and S1B) and Aurora 5L, with its lower sensitivity but full spectral information and unmixing algorithms, for their ability to resolve low levels of Tom in subsets of varying AF. The design of the antibody panel was based on the more limited conventional CytoFLEX LX 6L/ 21-color detectors' optical configuration. Fluorochromes with minimum spectral overlap with Tom were selected to avoid compensation or unmixing-derived spreading that could compromise the resolution of dim Tom signals. Spectrally quiet

fluorochrome choices were verified via three independent methods: 1. normalized spectra visualization based on Aurora data after FCS Express Ordinary Least Squares (OLS) unmixing (Figure 3A); 2. Fluorochrome Similarity™ Indices and overall panel Complexity™ Index (13) (Figure 3B); and 3. Flowjo SSM matrix after compensating single color references on the CytoFLEX (Figure 3C). An example of the lung gating strategy is shown in Figure 3D.

Cells expressing Tom appeared limited to AMΦ, αβT lymphocytes and CD45− fractions, when viewed against AF-correlating detector V610 (CytoFLEX) and V9 (Aurora) (Figure 4A and B). The choice of parameter to view Tom on a bi-variate plot was critical for AMΦ but not αβT Tom+ frequency determination (Figure 4D and E). AMΦ Tom+ were poorly resolved and displayed reduced frequencies when
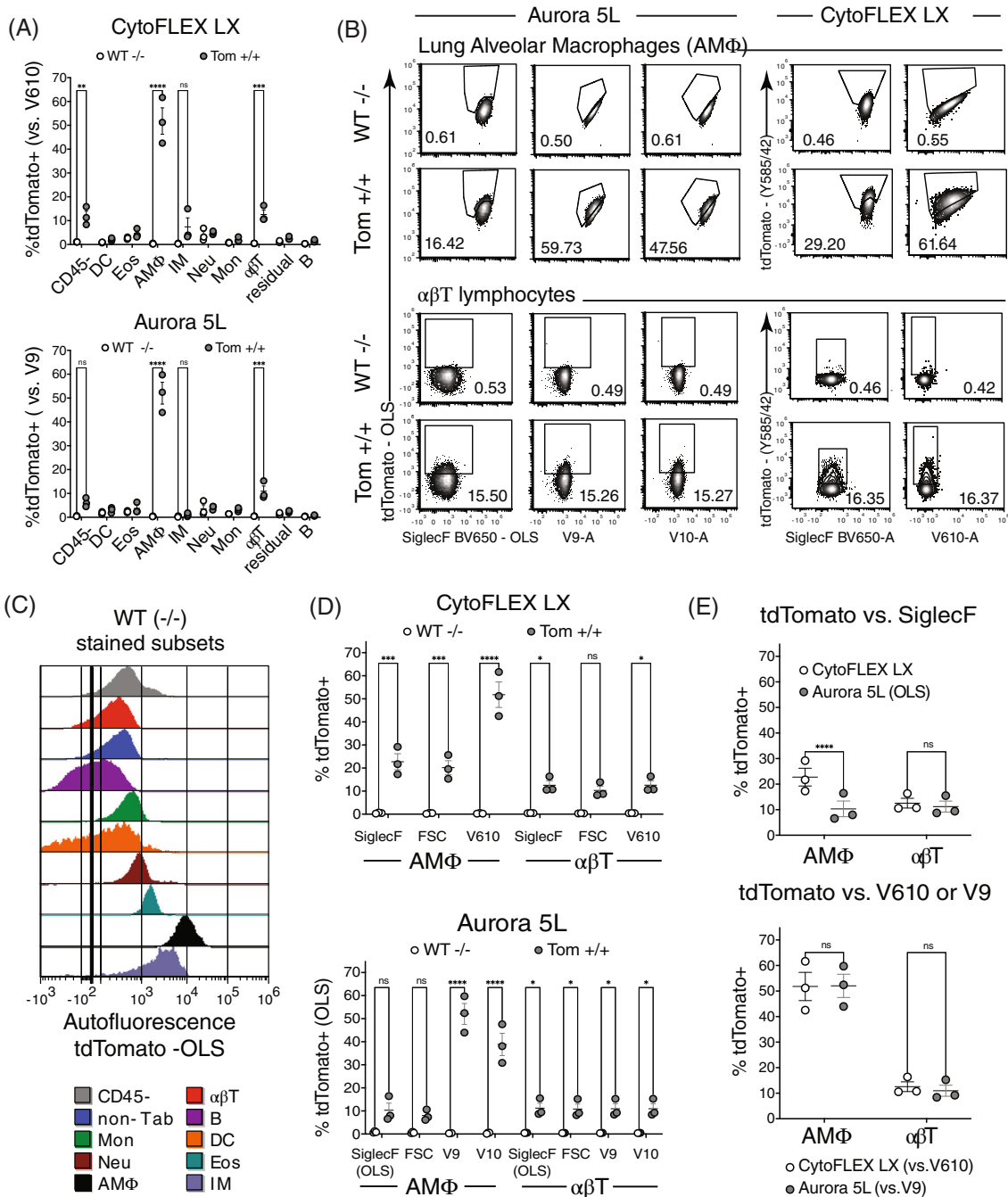
**FIGURE 4** Expression of tdTomato in lung resident cell subsets. (A) Comparison of Tom-expressing subsets in Tom+/+ vs WT mice in Aurora 5L and CytoFLEX LX. The subsets and frequencies expressing Tom are consistent between instruments: CD45− **$p < 0.01$, $\alpha\beta$T ***$p < 0.001$, AM$\Phi$ **** $p < 0.0001$ (ANOVA). (B and D) Impact of gating strategy on tdTom resolution AM$\Phi$ and $\alpha\beta$T cells. Resolution of tdTom dependent on the co-visualisation partner in 2D plots. V9 (Aurora) and V610 (CytoFLEX) resolved the highest frequencies of tdTom, Significant but lower frequencies were derived for other 2D visualisation partners $p < 0.05$, ***$p < 0.001$, **** $p < 0.0001$. (C) Autofluorescence (AF) profiles of stained lung WT (Tom−/−) subsets into the Tom channel after unmixing U. (E) Comparison of Aurora vs. CytoFLEX for resolution of subsets with different AF levels. On low AF background $\alpha\beta$T, Tom frequencies did not alter between Tom gating strategies: Tom versus SiglecF or Tom versus "AF detectors." On high AF background subset, AM$\Phi$ frequencies were masked when viewed on Aurora against SiglecF ($p < 0.0001$) [Color figure can be viewed at wileyonlinelibrary.com]

viewed against SiglecF BV650, or FSC but $\alpha\beta$T Tom$^+$ resolution and frequency were equally displayed against these alternate partner detectors (Figure 4D). To explore this phenomenon further, WT (Tom−/−) lung subsets were gated and analyzed after unmixing for

AF intensity in the Tom channel (Figure 4C). AM$\Phi$ (black histograms) displayed the highest AF in the Tom channel with MFI up to $3 \times 10^4$ while $\alpha\beta$T (red histograms) MFI in the Tom channel was 10-100-fold lower between $10^2$ and $10^3$. Given the high frequency of Tom
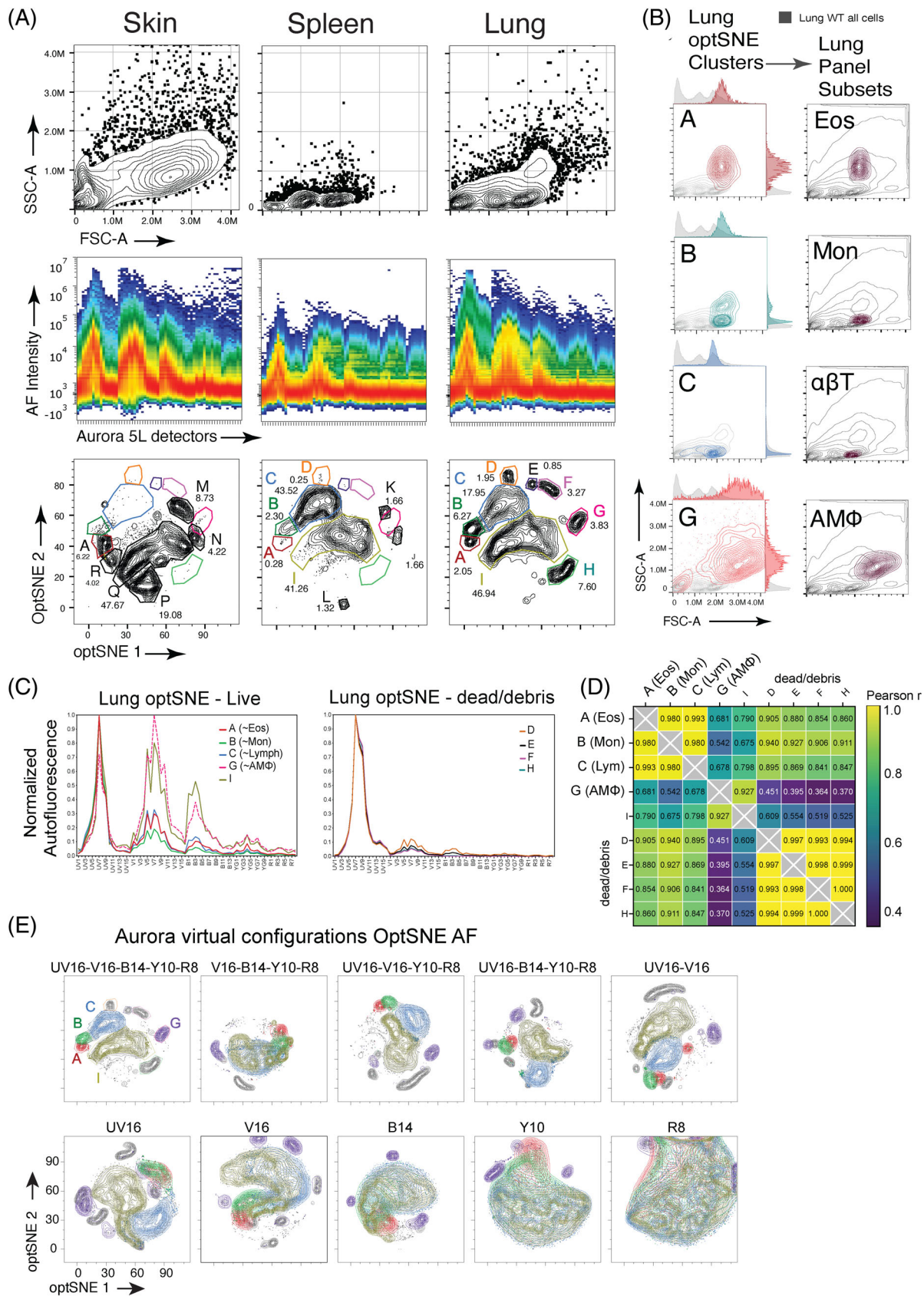
**FIGURE 5** Legend on next page.

expression by AMΦ and their high AF observed in CytoFLEX, we compared full spectrum unmixed Aurora data (using FCS Express OLS) against CytoFLEX compensated data in terms of Tom frequencies for both αβT lymphocytes and AMΦ, via bivariate plots using equivalent "AF detectors" V610 (CytoFLEX LX) and V9-10 (Aurora 5L). Remarkably, we observed significant AMΦ Tom$^+$ frequencies in Aurora matching CytoFLEX values when defined via 2D plots of Tom against raw Aurora parameters (Figure 4D and E) especially when correlated against "AF detector" V9 (405-598/20 nm). Significant but low levels of Tom expression were also observed in αβT cells with relative consistency across visualization methods. Hence, by careful selection of the parameters chosen to co-visualize Tom, including the simultaneous view of unmixed and raw AF detectors (a feature available in FCS Express but not the current version of SpectroFlo), the resolution hindering impact of AF can be overridden to reveal the presence of Tom$^+$ AMΦ in Aurora samples, with frequencies matching CytoFLEX results.

## 4.4 | High dimensional isolation of unique autofluorescent subsets

Our biological model offered an opportunity to evaluate the effect of full spectrum unmixing combined with AF extraction on the resolution of dim Tom on highly AF cells. Based on our results of fixed versus fresh lymphocyte analysis (Figure 2E), we extrapolated that the extraction of (specifically) AMΦ AF (values of ~10$^4$ in the Tom channel) would result in a substantial increase (~ 4-fold) in signal resolution. Before we could proceed with AMΦ-specific AF extraction, we needed to first generate a pure AF reference matching that of AMΦ. A typical workflow to generate subset-specific AF profiles would include the visualization of unstained events across multiple raw fluorescence detectors in $N \times N$ plots, isolate distinct AF subsets via sequential gating across several bivariate plots, evaluate spectral purity across Aurora 64 detectors and confirm the identity of AF candidates via scatter correlations with panel-defined cell subsets. This laborious approach also relies on the relatively high abundance of the subsets being considered and the ability to appropriately define parameter combinations that would result in pure spectral signatures.

As an alternative approach, we evaluated the utility of high dimensionality reduction algorithms (HiDi) to accurately resolve pure AF subsets in unstained samples based exclusively on their intensity across Aurora 5L 64 fluorescent detectors. In a preliminary attempt, representative unstained cells from the lung, skin and spleen of one WT mouse were concatenated and analyzed with opt-SNE (43) based

on all Aurora 5L fluorescence parameters in FlowJo. By this method, opt-SNE produced distinctive projections for each tissue, with the lung showing the greatest diversity of populations, some shared with spleen while showing minimal overlap with the skin (Figure 5A). Nine lung populations were manually gated (see Supporting Information, page 9) and analyzed for scatter profiles, AF (V7 vs. UV7) overlays with all events and spectral properties (Figure S11). Through similarities with scatter profiles of FCS files representing gated immunophenotyped lung subsets (Figure 5B), four opt-SNE populations, A, B, C and G, were identified as closely matching eosinophils, monocytes, lymphocytes and AMΦ, respectively. Another four populations (D, E, H and F) showed events exhibiting FSC values lower than lymphocytes, suggesting these were enriched for dead cells and debris (Figure S11B). Events within each gate also exhibited unique AF intensities and spectral signatures across Aurora detectors (Figures 5C and S11B). Of the opt-SNE populations analyzed, G (AMΦ) showed the highest AF values, between 10$^3$ and 10$^4$, across all detectors and a maximum at V7 (405 nm—542/17), contrasting with all other opt-SNE populations that shared a consistent maximum AF peak at UV7 (355 nm—514/28). Although opt-SNE populations including dead/debris events differed in their scatter profiles and AF intensities (Figure S11B), particularly among the UV and violet detectors, they exhibited almost identical normalized spectral profiles, with minor differences in the violet and blue channels (Figure 5C). The resolution of unstained cell populations with subtle differences in AF intensity or normalized spectra via opt-SNE was confirmed via a matrix of Pearson r correlations (Figure 5D); a statistic having an almost perfect linear correlation with Cytek Similarity™ Index ($R^2 = 0.9886$, $p < 0.001$, Figure S12). In contrast to the spectral uniqueness of the AMΦ (G), the opt-SNE populations resembling eosinophils (A), monocytes (B) and lymphocytes (C) where highly similar, based on Pearson r values (0.980–0.993). An even higher AF similarity was observed between dead/debris populations (Pearson r 0.993 to ~1.00), matching their normalized spectral profiles (Figure 5C). The reproducibility of these results was confirmed with 10 consecutive opt-SNE runs in FlowJo (Figure S13), showing consistent resolution for highly similar populations (A, B and C, for instance). Additionally, we evaluated how the number of lasers, their wavelengths and number of detectors affected the resolution of subsets by opt-SNE AF. To this end, we ran consecutive opt-SNE for several Aurora "virtual" laser configurations, including 1, 2, 4, or 5 lasers, by selecting their corresponding parameters from Aurora 5L's 64 detectors data (Figure 5E). The success of each opt-SNE run, in terms of the resolution of subtle AF differences between cells, for instance A from B (Pearson $r = 0.980$) or C from I (Pearson $r = 0.798$), was

**FIGURE 5** Resolution of Autofluorescence (AF) subsets via opt-SNE. (A) Scatter, spectra and opt-SNE projections of unstained lung, skin and spleen from one WT (Tom−/−) mouse acquired in Aurora 5L. Concatenated unstained cells from each tissue were analyzed by opt-SNE based on Aurora 5L 64 raw fluorescence parameters. (B) Populations were identified by comparison to scatter profiles of immunophenotyped lung hematopoietic subsets. (C) Normalized spectra of lung opt-SNE populations A–I. (D) Pearson r correlation matrix, as a measure of similarity between opt-SNE clusters. Population G showed the least similarity to any other AF subset identified. (E) Opt-SNE AF based on virtual configurations mimicking commercial available Aurora instruments or on detectors within single laser paths demonstrate the critical contribution of both UV and violet lasers (in combination with B,Y,R) in resolving AF clusters [Color figure can be viewed at wileyonlinelibrary.com]
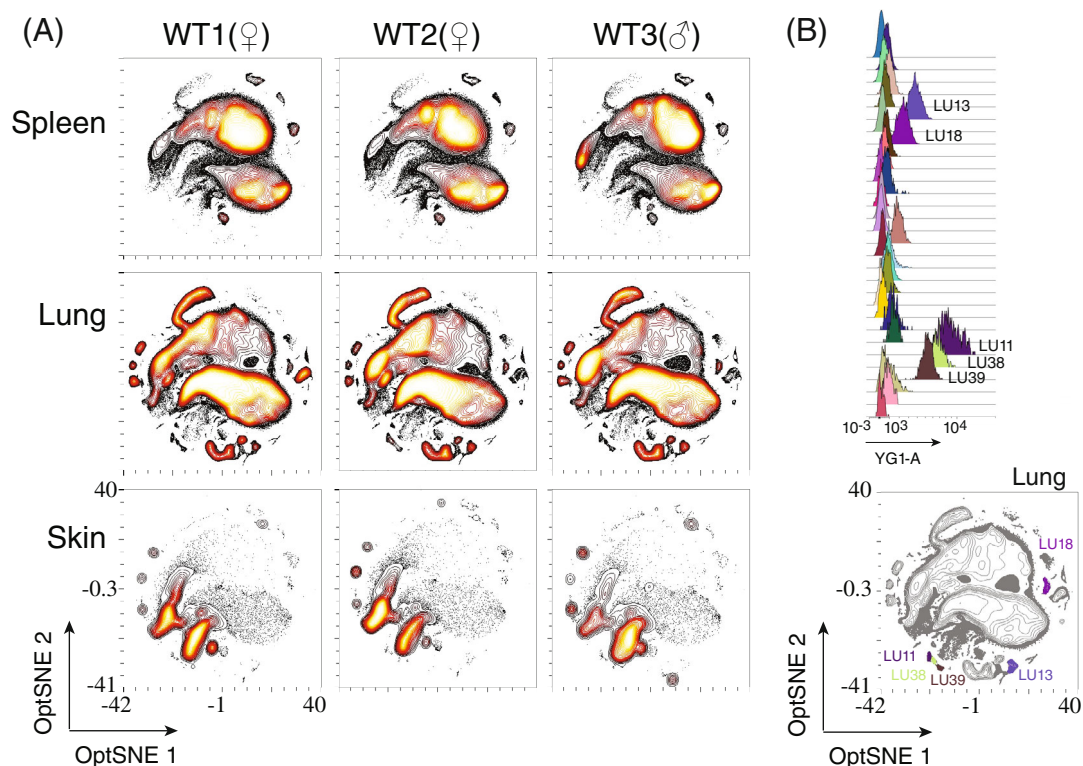
**FIGURE 6** Opt-SNE autofluorescence (AF) projections across tissues and replica mice. (A) OMIQ Opt-SNE AF projections of cells from spleen, lung and skin of female and male WT (Tom−/−) mice. (B) Highlighted Opt-SNE position and fluorescence intensity histograms of lung populations showing the highest AF at the YG-1 detector (tdTomato peak channel) [Color figure can be viewed at wileyonlinelibrary.com]

heavily dependent on the *simultaneous inclusion* of UV and Violet detectors. The relative higher importance of UV over V detectors was demonstrated by the opt-SNE AF improved success of 4L configurations including UV (UV-B-YG-R) over violet 4L counterparts (V-B-YG-R). Populations' resolution within projections was lost when opt-SNE was exclusively based on UV or V detectors. Similar loss of resolution was seen with opt-SNE in other Aurora laser configurations such as 3L (B14-YG14-R8) (not shown). The relevance of UV and Violet detectors in the successful opt-SNE resolution of leukocyte AF subsets is not surprising, given their diversity in terms of intensity and spectral signatures along these regions (Figure 5C).

The use of opt-SNE AF in AF discovery was further exploited to identify rare cell subsets across tissues and replicas. For this, Aurora FCS files containing unstained WT lung, spleen and skin cells from one male and two female mice (nine samples total) were uploaded to the online OMIQ data analysis software. Cleaned data were gated for singlets and subsampled to include $3 \times 10^5$ events per lung and spleen, ~ $5 \times 10^4$ from skin before running opt-SNE based on Aurora 64 fluorescence parameters. The results confirmed our preliminary findings: shared opt-SNE populations between lung and spleen, highest opt-SNE projection complexity in lung, and little similarity of these organs to skin (Figure 6A). Manual gating (Figure S14) was used to comprehensively define ~70 AF populations based on their opt-SNE resolution and relative abundance across tissues and replicates. The analysis of opt-SNE by

mouse and tissue revealed consistency in overall tissue specific projections (Figure 6A) but small changes in relative population frequencies (Figure S15B). For example, higher similarities were observed between the female mouse replicas, while diverging from the male in the relative abundance of some of minor populations (Figure 6A and Figure S15B). Relevant to our Tom reporter discovery project, we identified five populations in WT lung showing distinctive medium (LU13 and 18) to high AF levels (LU 11, 38, 39, ~ AMΦ) at the YG1 detector. Their opt-SNE positions and YG1 AF intensities are shown in Figure 6B.

As a proof of principle to discovery projects in disease models, we further tested the potential of opt-SNE AF to both assess the consistency between replica samples in mice within a given experimental group and reveal differences in AF profiles in tissue samples from mice undergoing a major immunological event. The analysis included unstained samples acquired in Aurora 5L as part of immunophenotyping experiments for two experimental mouse models established at the University of Melbourne. In one instance, unstained cells from the visceral adipose tissue, spleen, and bone marrow of two groups of mice (five each) fed with different diets (A and E) were analyzed via OMIQ opt-SNE. The results showed consistency in opt-SNE projections among replica mice within each group, the similarities in overall tissue profile across diet regimes and the differences in opt-SNE projections between tissues (Figure S16). In the second animal model, opt-SNE AF projections
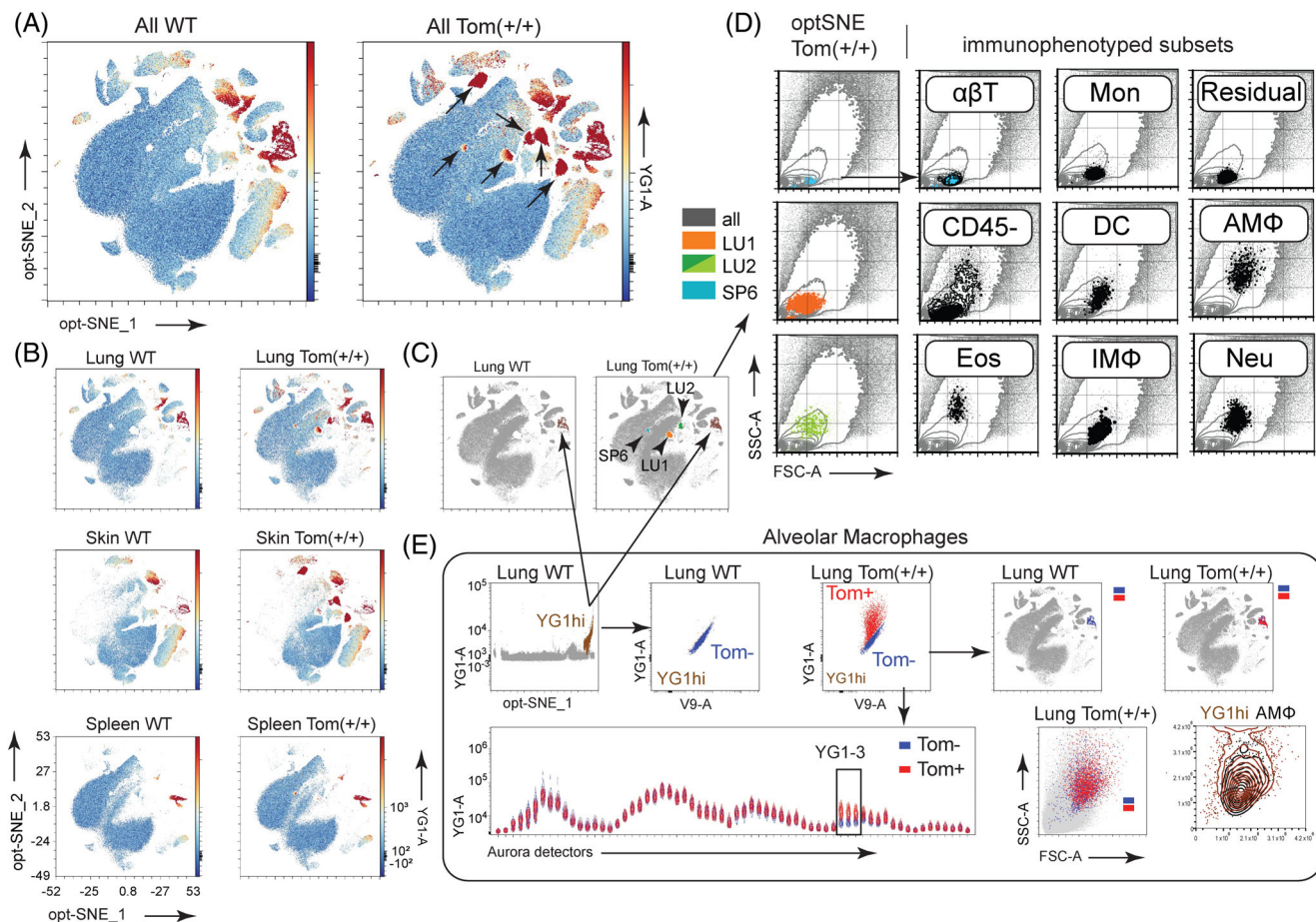
**FIGURE 7** Opt-SNE of unstained, concatenated Tom+/+ and WT files identifies unique Tom subsets. (A) Concatenated files of WT and Tom+/+ lung, skin and spleen analyzed via OMIQ opt-SNE reveal six Tom+/+ mice-specific populations (black arrows) showing increased YG1 intensities (peak channel for Tom). (B-C) Highlighted Tom populations on opt-SNE projections of skin, spleen and lung, where three Tom+/+ mice-specific populations were identified: LU1, LU2, and SP6. (D) Attempted identification of tdTom populations LU1, 2 and SP6 by overlay onto lung scatter plots of immunophenotypically-defined cells. SP6 corresponds to αβT. LU1 and LU2 resemble but not correspond to defined cell subsets. (E) High YG1 AF populations in WT and Tom+/+ Opt-SNE identified as AMΦ by overlay onto immunophenotyped AMΦ scatter plot. Opt-SNE AF could not distinguish between Tom+ and Tom− AMΦ in tdTom mice [Color figure can be viewed at wileyonlinelibrary.com]

of kidney, liver, salivary glands (SG) and spleens from WT mice were evaluated 30 days after infection with two variants of the lympho-cytic choriomeningitis virus (LCMV): Armstrong (acute) vs. CL13 (chronic). In this model, stark differences in opt-SNE AF, scatter and global spectral projections in all tissues were observed in chronic vs acute LCMV infected mice (Figures S17 and S18). These dramatic changes in AF projections could be evidence of changes in the diversity or frequency of tissue resident cell subsets, or an indica-tion of phenotypic and metabolic changes in these resident cells, which are both potentially overlooked by the immunophenotyping panel used to assess this model. Opt-SNE-enabled comprehensive autofluorescence exploration of complex cellular mixes including subsets exhibiting highly similar spectral profiles, was appreciated in its capacity to distinguish subsets that although exhibiting unique AF signatures (and scatter profiles) cannot be fully resolved via the visualization of fluorescence histograms or bivariate plots (Figure S19). We wanted to know if other high-dimensionality reduction algorithms resolved leukocyte AF to a similar degree,

focusing on UMAP, an algorithm differing from opt-SNE in terms of speed (faster), projection consistency across runs and higher emphasis on "global" over "local" data structure (44). Figure S20 shows the results from 30 UMAP runs based on combinations of *number of neighbors* (5, 15, 30, 50, and 100) and minimum distance parameters (0, 0.02, 0.05, 0.1, 0.4 and 1). Remarkably similar pro-jections representing a continuum of mostly unresolved events were observed in all cases (Figure S20A). We explored the fate of manually gated opt-SNE populations via contour overlays against UMAP projections of the same data (Figure S19). These opt-SNE populations, including cells with close AF spectra (Person *r* from 0.9250 to 0.9956) and distinct scatter profiles were revealed to occupy contiguous segments within the UMAP projections (Figure S20B), their relative location corresponding to their Pearson *r* similarity values, but failing to resolve into isolated populations at the level provided by opt-SNE (Figure S19A).

Finally, we mused that the ability of opt-SNE AF to unmask subtle AF correlations could be used to discover additional Tom-
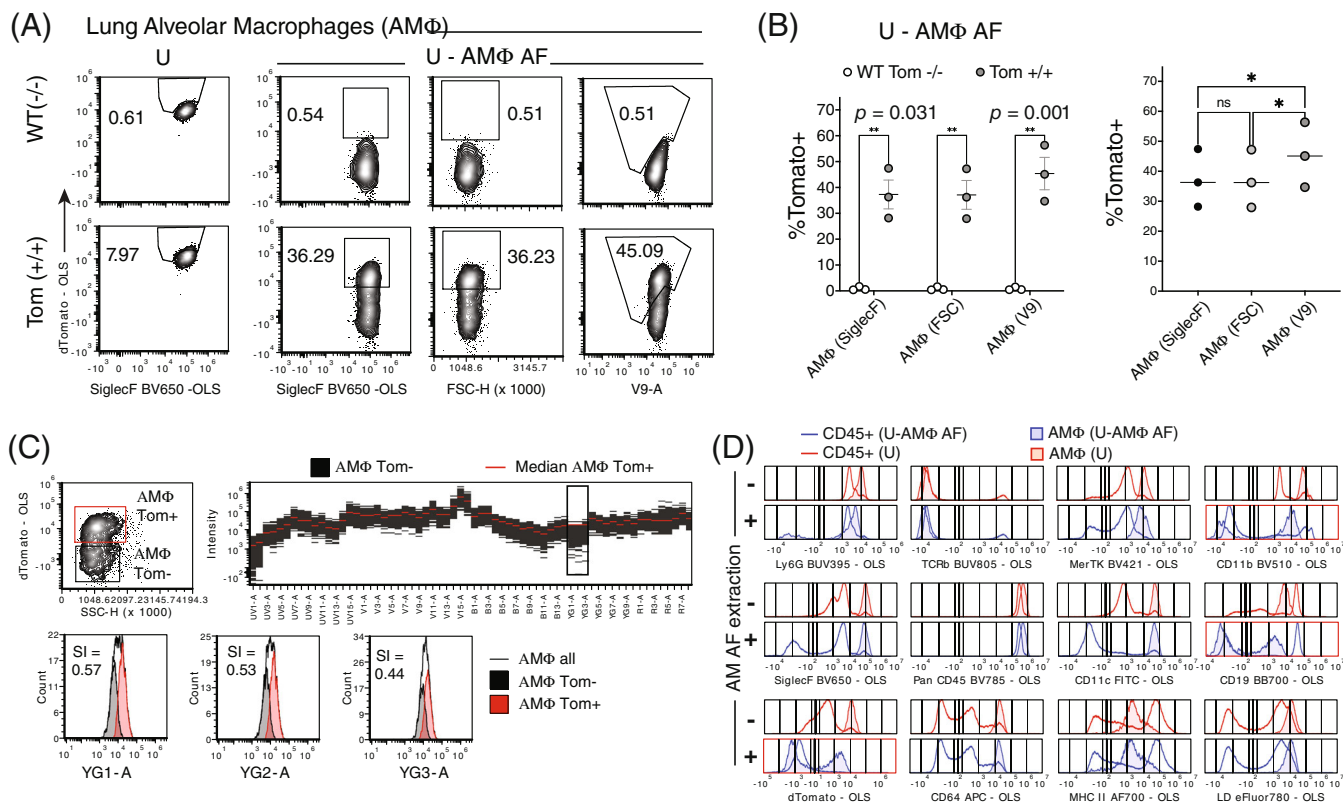
**FIGURE 8** Unmixing with AMΦ-specific autofluorescence (AF) extraction resolves Tom+ AMΦ by Aurora. (A) Example of AMΦ Tom resolution changes co-visualized against other channels (as Figure 4B) after U versus U-AF. (B) Significant **p < 0.05 and almost equal expression of Tom on Tom+/+ AMΦ (top) after AMΦ-specific AF extraction regardless of gating strategy (bottom). (C) Spectral traces of gated Tom+ and Tom− AMΦ highlighting positive events in best resolved raw detectors (YG1, YG2, and YG3). High level of overlap reflected in very low SI across 'best resolved' detectors. (D) Fluorescence distributions of AMΦ and total CD45+ events after U and U-AMΦ AF. U-AMΦ AF 'corrects' marker expression by AMΦ for CD11b, CD19 and marginally Ly6G markers attached to fluorochromes that had most spectral overlap from AMΦ AF in violet, blue and UV detectors respectively [Color figure can be viewed at wileyonlinelibrary.com]

expressing subsets in skin, lung and spleen to those already identified using immunophenotyped samples. We hypothesized that the incorporation of Tom fluorescence to the WT AF spectra should lead to Tom (+/+) mice-specific populations absent from WT tissue samples. To test this, 50,000 unstained cells each from the skin, spleens and lungs of three WT and Tom+/+ mice were concatenated and analyzed by opt-SNE in OMIQ. Comparing opt-SNE projections of concatenated WT vs Tom+/+ samples, highlighted via heatmap plots based on YG1-A intensities identified six populations unique to Tom+/+ mice (Figure 7A). Five of these populations were present in Tom+/+ skin, two in spleen and three in lung (Figure 7B). Tom-specific populations found in lung (LU1, LU2, and SP6) were exported as FCS files and their scatter distribution compared against FCS files of exported gates of each immunophenotyped lung subset. SP6 events and αβT lymphocytes scatter profiles were identical, while LU1 and LU2 events' scatter suggested they were part of the CD45− gated events (Figure 7C-D). Curiously, despite AMΦ being the subset with the highest percentage of Tom expression (Figure 4A), Tom positive and negative AMΦ were not resolved by opt-SNE, found to collocate within the same opt-SNE projection's region, shared by WT and Tom mice

(Figure 7C). The AMΦ opt-SNE population was identified based on WT AMΦ's high AF in the YG1 detector, confirmed by an exact overlay with panel-defined AMΦ scatter reference and Tom expression in YG1 versus V9 plots (Figure 7E). The spectral differences between Tom+ and Tom− AMΦ were minimal, restricted to the first three detectors of the 561 nm laser path, where both populations failed to fully resolve, demonstrating the overwhelming masking effect of specific Tom signals by AMΦ AF.

## 4.5 | Subset-specific autofluorescence extraction resolves tom+ alveolar macrophages

Our biological question to date has sought to determine the expression and tissue distribution of our rare immunological protein represented by the surrogate expression of Tom in mouse tissues. Our efforts to this end lead us to the mathematical understanding of the negative impact of AF on signal resolution, to the definition of AF intensity ranges anticipating resolution improvements after unmixing with AF extraction and a new workflow to isolate pure subset-specific AF reference files (or tags). Having determined that AF extraction

from AMΦ would provide the most benefit for Tom resolution, we used opt-SNE AF, to isolate, define and verify a pure spectral reference for AMΦ AF in FCS Express (Figure S21). The identified population was exported as an FCS file and used as AF reference for AMΦ-specific U-AF of lung WT and Tom+/+ Aurora samples via OLS with FCS Express. Henceforth, AMΦ- specific unmixing and AF extraction is written as U- AMΦ AF. As shown in Figure 8A (top row), U- AMΦ AF led to a dramatic reduction in WT AMΦ MFI values at the unmixed Tom OLS channel, improving the resolution (bottom row) of Tom$^+$ from Tom$^-$ AMΦ in Tom+/+ mice and increasing the percentage of Tom$^+$ AMΦ detected over U-only results. Significant AMΦ Tom$^+$ frequencies were observed regardless of visualization strategy (Tom vs. FSC or SiglecF-OLS), although frequency values across mouse replicates (~28%, 36%, and 47%) were still significantly lower than tdTom-OLS vs raw detector V9-derived results (35%, 45%, and 56%, Figure 8B). The power of subset-specific U- AMΦ AF was on full display, resolving Tom$^+$ and Tom- AMΦ populations otherwise undistinguishable via opt-SNE or in U-only parameter data. Taking advantage of the ability of FCS Express to preserve raw parameters in unmixed FCS files, we explored the raw data spectral distribution and YG1-3 histogram overlay of *stained* AMΦ tdTom$^+$ and tdTom$^-$ populations defined after U-AMΦ AF, revealing just how marginal these differences in the first three detectors at the 561 nm laser path are (YG1-3 ~ Tom emission maximum), with positive and negative populations failing to fully resolve (Stain index 0.44–0.57, Figure 8C).

Including AMΦ AF as a new fluorophore in our antibody panel could compromise data quality due to unanticipated spectral similarities between the newly added AF reference and the original panel fluorochromes, leading to spreading errors after unmixing, particularly where there is high similarity between fluorophores. In terms of spectral similarity, we found AMΦ AF spectral signatures closely matched BV510 (Pearson $r = 0.94$), already assigned in our lung panel to CD11b, while showing no similarity with Tom (Pearson $r = -0.01$) or other panel fluorochromes (Figure S22). Although the spreading around AMΦ CD11b$^-$ populations after AF extraction (Figure 8D) could derive from spectral similarities between BV510 and AMΦ AF, the observed spreading around the negatives in CD19-BB700 and Ly6G-BUV395, with minimum spectral similarities with AMΦ AF, suggest this is not the dominant factor. As shown in the CD4-stained fixed vs fresh blood unmixing experiments (Figures 2C and S10), AF extraction invariably leads to the increase of spreading around the negative populations, since the limited reduction in negative population variances observed after unmixing with AF extraction, coupled to a substantial reduction in the MFI for this population contributes to a large coefficient of variation. The removal of AMΦ AF also led to a "phenotypic correction" of the AMΦ subset, particularly in the CD19, Ly6G and CD11b parameters, by removing the creep of the AF component of AMΦ into BB700, BUV395 and BV510, respectively. We observed no notable changes in the intensity and distribution for the remaining markers, thereby confirming the AMΦ phenotype as CD45$^{hi}$ SiglecF$^{hi}$ CD11c$^{hi}$ CD64$^{hi}$ MHCII$^{lo-hi}$ Ly6G$^{+/-}$(Figure 8D).

# 5 | DISCUSSION

Immunophenotype discovery projects unveiling the expression, subset and tissue distribution of poorly characterized proteins pose technical challenges. The unifying concern guiding all our empirical recipes for successful measurement of key rare and dim markers is the understanding of the factors that enhance and dampen resolution. As shown here, when it comes to the fundamental players driving resolution in cytometry, AF as much as instrument sensitivity parameters ($Q$ and $B$) must be included as a major influence.

Although fluorochrome operational brightness is affected by the instrument's sensitivity parameters and the intrinsic properties of fluorochromes (extinction coefficient and quantum yield), we demonstrated that it also depends on the AF of the cells. Variations in carrier AF produce drastic changes in fluorochrome brightness ranking and resolution trends across detectors, a practical illustration of the validity of Equations (13) and (14). A fluorochrome operationally defined as "bright" on fresh cells, will appear dimmer when measured on fixed cells or cells with higher intrinsic AF in spectral regions matching the fluorochrome's emission. Therefore, an understanding of the unique AF properties of the cellular subsets included in a study, together with the monitoring of AF changes in longitudinal studies, or the overall impact of fixation protocols on baseline AF are all necessary to avoid compromising the quality of cytometric data.

Another important aspect of AF is its relationship with instrument sensitivity. As far as we are aware, this is the first time that AF is explicitly considered in the context of modern cytometry sensitivity equations as a particle-born fluorescence signal on its own. We have demonstrated that the dependency of measurement precision (*CV*) on sensitivity factors ($Q$ and B) decreases at high levels of AF. At high AF intensity, the resolution of fluorescent and "unstained" populations can be demonstrated to be no longer dependent on instrument sensitivity factors ($Q$ and $B$) and thus, cytometers of varying intrinsic sensitivity ($Q > 0$) will produce similar resolution outcomes (Equations S1–S6). Although instrument's sensitivity parameters ($Q$ and $B$) remain critical for the resolution of dim signals, the enhanced performance of a sensitive instrument will be best witnessed in low AF settings explaining why differences across instruments in the resolution of CD4 in fresh blood or Rainbow dim peaks would not translate into equivalent differences in the resolution of Tom in AMΦ. Although Equation (5)–(16) are used here to elucidate the effect of AF on signal measurement precision and fluorescence resolution, these equations will equally apply to other particle-associated background sources contaminating the measurement of fluorochrome-derived photons. Similar effects on measurement CV and fluorescence resolution can derive from chemical fixation, staining with structural and viability dyes or unblocked particle scatter, among other examples.

Sensitivity-aimed strategies to enhance the definition of rare makers in phenotype discovery projects although benefiting cells of low AF (αβ T cells), will not avoid the resolution hindrance affecting fluorescence measurements on highly AF cells (AMΦ), as shown in this study. Indeed, after designing a fluorochrome panel to minimize the impact of spreading into the crucial Tom channel in the case of these

reporter mice, and evaluating samples in instruments with high sensitivity, the problem of AMΦ AF remained, unavoidably affecting Tom resolution. To overcome this issue, a thorough exploration and even exploitation of AF properties was required to efficiently isolate and remove subset AF to correct its negative contribution to Tom measurements.

This is where full spectrum unmixing with AF extraction comes to the fore. U-AF increases the dynamic range or SI by reducing the negative population's MFI and is most noticeable and appreciated when applied to highly AF cell types such as fixed lymphocytes or AMΦ. As shown in the evaluation of CD4 stain index after unmixing, resolution outcomes after AF extraction bears the balance of two opposite effects: the increase in the separation of negative and positive events and the spreading generated around the negative population. Based on fixed and fresh blood results, the strongest improvements in SI after AF extraction correlated with the higher AF content of the unmixed negative populations. Based on the modest improvement of CD4 SI after U-AF in fresh lymphocytes, these cells could be used as intensity references in the estimation of the relative levels of AF carried by other leukocyte subsets within a sample before deciding whether to apply AF extraction.

Another factor to consider while evaluating the expression of dim fluorescent signals on highly AF cells is the unmixing software of choice and its limitations. In SpectroFlo software, all raw channels are removed after unmixing and unmixed FCS files are limited to the number of individual fluorochromes included in the reference list. As demonstrated by CytoFLEX, when visualized against "AF" detector V610, AMΦ expressed the highest levels of Tom across all lung subsets. However, the same expression pattern was not observed when acquired on Aurora and assessed via unmixed detectors by SpectroFlo or FCS Express. In contrast to SpectroFlo, an additional FCS Express feature that preserves raw parameters after unmixing allowed us to re-evaluate unmixed Tom expression in AMΦ via 2D plots against AF-correlating raw detectors (V9 and V10). This approach revealed Tom+ AMΦ percentages in Aurora match CytoFLEX results. Users must be aware of this shortcoming of the SpectroFlo software, and we recommend applying a 'second opinion' from independent software to avoid premature conclusions on the phenotype of highly AF cells. Absence of marker resolution on highly AF populations in SpectroFlo unmixed data does not necessarily correlate with the absence of a marker's signal in raw files.

A major challenge in phenotype discovery projects is the inconsistency in the measurements of rare markers across subsets of varying AF. Although the phenotype discovery work presented here focused on the lung, as a model of Tom expression in both low and high AF subsets, the study also aimed to evaluate Tom expression in skin and spleen subsets and the use of U-AF as a strategy to correct for AF-driven inconsistencies. As shown, the relative AF intensity of subsets correlated positively with resolution improvements after AF extraction and the level of AF intensity could be inferred from the MFI of the unmixed negative populations along the Tom channel or relative to lymphocyte and AMΦ AF levels. Once the populations with high AF had been identified, a mandatory step before applying subset specific U-AF algorithms was the generation of single color file references

matching the intrinsic AF of the relevant panel cell subsets. The currently recommended procedure to isolate pure AF references in Aurora, called "Discover, Distinguish and Designate" (DDD), involves the isolation of unique AF subsets in unstained samples via their progressive evaluation of $N \times N$ plots based on raw FCS fluorescence parameters, aided by the inspection of scatter profile consistency and full spectrum purity of gated AF candidates. Although this manual approach easily enables the isolation of references for populations with unique AF profiles such as AMΦ, it becomes increasingly laborious if applied to the isolation of all potentially relevant AF subsets in a study. As an alternative approach facilitating the discovery of unique AF subsets, we made use of the inherent power of dimensionality reduction algorithms to successfully resolve AF complexity across Aurora 64 fluorescence detectors into a two-dimensional map of defined AF subsets. As far as we are aware, this is the first reported instance of the application of high-dimensionality reduction algorithms to the label free dissection of unique AF signatures in complex mammalian cell mixtures.

The benefits of evaluations over multiple dimensions, as a strategy that overcomes the resolution limitations of a single parameter, is already illustrated in the stark differences in tdTom+ AMΦ resolution in 2D plots based on unmixed parameters or AMΦ AF versus single dimension histograms for tdTom. Applying this principle to Aurora 5L, providing a detailed measurement of AF emission across 64 detectors, the benefits of AF discovery via dimensionality reduction algorithms over manual approaches is evident for the potential to isolate seemingly unresolvable subsets of subtle differences in AF. As shown here, opt-SNE projections consistently enable the distinction of pure AF profiles of high similarity representing biologically relevant cell subtypes. We cannot conclude at this point whether the observed differences between UMAP and opt-SNE projections could be minimized via an exhaustive evaluation of parameter combinations for UMAP beyond those evaluated here, or a reflection on the algorithms' differences in the handling of AF "local" vs. "global" data structure. Since the spectral differences between opt-SNE resolved AF populations are consistent but sometimes minimal, an algorithm' emphasis on local data structure seems important in the resolution of closely related AF subsets. Given the AF similarities observed between leukocyte populations, it is not surprising that laser configuration and the number of parameters included in the analysis affect opt-SNE outcome. Our analysis of opt-SNE projections based on virtual Aurora configurations, revealed the critical requirement of UV and violet lasers in combination for the resolution of mouse AF subsets, and should be considered critical when making instrument configuration choices for this type of analysis. The UV and V configuration dependency of opt-SNE is explained by the AF spectral signature of the samples used in the evaluation, showing the most noticeable differences along these regions. Interestingly, and illustrating the dependency of AF discovery success on high dimensional measurements, neither UV or violet detectors alone can resolve AF at the level provided by opt-SNE projections where additional lasers and detectors were included.

We have demonstrated that opt-SNE resolves AF subsets with a high level of spectral purity, reveals differences in the AF fingerprint of tissues, demonstrates replica consistency in fasting models and highlights minor differences as between female and male mice. When applied to the evaluation of viral infection, drastic changes in AF makeup per tissue were revealed. Ongoing studies will attempt to understand how these AF changes correlate with changes in subset phenotypes, via AF population frequency and scatter correlations with populations identified via immunophenotyping. Beyond this, the analysis of label-free opt-SNE AF projections could be used to reveal differences in specific cell subset yield as a function of sample preparation and to highlight relevant cellular subsets in a sample undergoing changes in frequency or AF phenotype in support of targeted polychromatic studies. As illustrated here, opt-SNE based on AF measurements can be used as an exploratory technique in phenotype discovery projects involving the definition of all relevant subsets expressing a fluorescence protein-based gene reporter.

Together, our data mathematically and empirically explain the "yin and yang" of AF in signal resolution by flow cytometry and demonstrate a novel, time-saving approach using HiDi reduction algorithms to isolate subset AF signatures leading to its removal from fluorescent measurements, to globally identify novel cellular subsets, subtle and major AF differences in homeostasis and following immunological challenges in a variety of living contexts.

## AUTHOR CONTRIBUTIONS

**Vanta Jameson:** Conceptualization (supporting); data curation (supporting); formal analysis (supporting); investigation (equal); writing – original draft (equal); writing – review and editing (lead). **Tina Luke:** Investigation (supporting). **Yuting Yan:** Investigation (supporting). **Angela Hind:** Investigation (supporting). **Maximilien Evrard:** Investigation (supporting); resources (supporting); writing – review and editing (supporting). **Kevin Man:** Investigation (supporting); resources (supporting). **Laura K Mackay:** Funding acquisition (supporting); resources (supporting). **Axel Kallies:** Funding acquisition (supporting); resources (supporting); writing – review and editing (supporting). **Jose A Villadangos:** Funding acquisition (supporting); resources (supporting). **Hamish E. G. McWilliam:** Conceptualization (supporting); data curation (equal); formal analysis (equal); funding acquisition (lead); investigation (supporting); methodology (supporting); project administration (lead); resources (lead); software (supporting); supervision (lead); validation (supporting); visualization (supporting); writing – original draft (supporting); writing – review and editing (supporting). **Alexis Perez-Gonzalez:** Conceptualization (lead); data curation (lead); formal analysis (lead); investigation (lead); methodology (lead); project administration (lead); software (lead); supervision (lead); writing – original draft (lead); writing – review and editing (lead).

## PEER REVIEW

The peer review history for this article is available at https://publons.com/publon/10.1002/cyto.a.24555.

## ORCID

*Alexis Perez-Gonzalez* https://orcid.org/0000-0002-8674-2034

## REFERENCES

1. Maecker HT, Frey T, Nomura LE, Trotter J. Selecting fluorochrome conjugates for maximum sensitivity. Cytometry A. 2004;62:169–73.
2. Bigos M. Separation index: an easy-to-use metric for evaluation of different configurations on the same flow cytometer. Curr Protoc Cytom. 2007;Chapter 1:Unit1.21.
3. Wood JC. Fundamental flow cytometer properties governing sensitivity and resolution. Cytometry. 1998;33:260–6.
4. van den Engh G, Farmer C. Photo-bleaching and photon saturation in flow cytometry. Cytometry. 1992;13:669–77.
5. Chase ES, Hoffman RA. Resolution of dimly fluorescent particles: a practical measure of fluorescence sensitivity. Cytometry. 1998;33:267–79.
6. Hoffman RA, Wood JC. Characterization of flow cytometer instrument sensitivity. Curr Protoc Cytom. 2007;Chapter 1:Unit1.20.

7. Parks DR, el Khettabi F, Chase E, Hoffman RA, Perfetto SP, Spidlen J, et al. Evaluating flow cytometer performance with weighted quadratic least squares analysis of LED and multi-level bead data. Cytometry A. 2017;91:232–49.

8. Wood JC, Hoffman RA. Evaluating fluorescence sensitivity on flow cytometers: an overview. Cytometry. 1998;33:256–9.

9. Wood JCS. How well can your flow cytometer detect photons? Cytometry A. 2021;99:664–7.

10. Wang L, Gaigalas AK, Abbasi F, Marti GE, Vogt RF, Schwartz A. Quantitating fluorescence intensity from fluorophores: practical use of MESF values. J Res Natl Inst Stand Technol. 2002;107:339–53.

11. Steen HB. Noise, sensitivity, and resolution of flow cytometers. Cytometry. 1992;13:822–30.

12. Bhowmick D, Sheridan RTC, Bushnell TP, Spalding KL. Practical guidelines for optimization and characterization of the Beckman coulter CytoFLEX™ platform. Cytometry A. 2020;97:800–10.

13. Park LM, Lannigan J, Jaimes MC. OMIP-069: forty-color full Spectrum flow cytometry panel for deep Immunophenotyping of major cell subsets in human peripheral blood. Cytometry A. 2020;97:1044–51.

14. Nguyen R, Perfetto S, Mahnke YD, Chattopadhyay P, Roederer M. Quantifying spillover spreading for comparing instrument performance and aiding in multicolor panel design. Cytometry A. 2013;83:306–15.

15. Perfetto SP, Chattopadhyay PK, Roederer M. Seventeen-colour flow cytometry: unravelling the immune system. Nat Rev Immunol. 2004;4:648–55.

16. Ferrer-Font L, Small SJ, Lewer B, Pilkington KR, Johnston LK, Park LM, et al. Panel optimization for high-dimensional Immunophenotyping assays using full-spectrum flow cytometry. Curr Protoc. 2021;1:e222.

17. Duan M, Li WC, Vlahos R, Maxwell MJ, Anderson GP, Hibbs ML. Distinct macrophage subpopulations characterize acute infection and chronic inflammatory lung disease. J Immunol. 2012;189:946–55.

18. Lohmeyer J, Friedrich J, Rosseau S, Pralle H, Seeger W. Multiparameter flow cytometric analysis of inflammatory cells contained in bronchoalveolar lavage fluid. J Immunol Methods. 1994;172:59–70.

19. Mosiman VL, Patterson BK, Canterero L, Goolsby CL. Reducing cellular autofluorescence in flow cytometry: an in situ method. Cytometry. 1997;30:151–6.

20. Surre J, Saint-Ruf C, Collin V, Orenga S, Ramjeet M, Matic I. Strong increase in the autofluorescence of cells signals struggle for survival. Sci Rep. 2018;8:12088.

21. Roederer M, Murphy RF. Cell-by-cell autofluorescence correction for low signal-to-noise systems: application to epidermal growth factor endocytosis by 3T3 fibroblasts. Cytometry. 1986;7:558–65.

22. Shi L, Lu L, Harvey G, Harvey T, Rodríguez-Contreras A, Alfano RR. Label-free fluorescence spectroscopy for detecting key biomolecules in brain tissue from a mouse model of Alzheimer's disease. Sci Rep. 2017;7:2599.

23. Yakimov BP, Gogoleva MA, Semenov AN, Rodionov SA, Novoselova MV, Gayer AV, et al. Label-free characterization of white blood cells using fluorescence lifetime imaging and flow-cytometry: molecular heterogeneity and erythrophagocytosis [invited]. Biomed Opt Express. 2019;10:4220–36.

24. Mitchell AJ, Pradel LC, Chasson L, van Rooijen N, Grau GE, Hunt NH, et al. Technical advance: autofluorescence as a tool for myeloid cell analysis. J Leukoc Biol. 2010;88:597–603.

25. Malkassian A, Nerini D, van Dijk MA, Thyssen M, Mante C, Gregori G. Functional analysis and classification of phytoplankton based on data from an automated flow cytometer. Cytometry A. 2011;79:263–75.

26. Zeng Y, Xu J, Li D, Li L, Wen Z, Qu JY. Label-free in vivo flow cytometry in zebrafish using two-photon autofluorescence imaging. Opt Lett. 2012;37:2490–2.

27. Steinkamp JA, Stewart CC. Dual-laser, differential fluorescence correction method for reducing cellular background autofluorescence. Cytometry. 1986;7:566–74.

28. Smith CA, Pollice A, Emlet D, Shackney SE. A simple correction for cell autofluorescence for multiparameter cell-based analysis of human solid tumors. Cytometry B Clin Cytom. 2006;70:91–103.

29. Sebestyén Z, Nagy P, Horváth G, Vámosi G, Debets R, Gratama JW, et al. Long wavelength fluorophores and cell-by-cell correction for autofluorescence significantly improves the accuracy of flow cytometric energy transfer measurements on a dual-laser benchtop flow cytometer. Cytometry. 2002;48:124–35.

30. Dashkova V, Clapper J, Vorobjev IA, Barteneva NS. Spectral and imaging flow cytometry in phytoplankton research. Methods Mol Biol. 2018;1745:83–95.

31. Grégori G, Rajwa B, Patsekin V, Jones J, Furuki M, Yamamoto M, et al. Hyperspectral cytometry. Curr Top Microbiol Immunol. 2014; 377:191–210.

32. Novo D, Grégori G, Rajwa B. Generalized unmixing model for multispectral flow cytometry utilizing nonsquare compensation matrices. Cytometry A. 2013;83:508–20.

33. Roederer M. Spectral compensation for flow cytometry: visualization artifacts, limitations, and caveats. Cytometry. 2001;45:194–205.

34. Robinson JP. Spectral flow cytometry-quo vadimus? Cytometry A. 2019;95:823–4.

35. Roca CP, Burton OT, Gergelits V, Prezzemolo T, Whyte CE, Halpert R, et al. AutoSpill is a principled framework that simplifies the analysis of multichromatic flow cytometry data. Nat Commun. 2021;12:2890.

36. Niewold P, Ashhurst TM, Smith AL, King NJC. Evaluating spectral cytometry for immune profiling in viral disease. Cytometry A. 2020; 97:1165–79.

37. Futamura K, Sekino M, Hata A, Ikebuchi R, Nakanishi Y, Egawa G, et al. Novel full-spectral flow cytometry with multiple spectrally-adjacent fluorescent proteins and fluorochromes and visualization of in vivo cellular movement. Cytometry A. 2015;87:830–42.

38. Schmutz S, Valente M, Cumano A, Novault S. Spectral cytometry has unique properties allowing multicolor analysis of cell suspensions isolated from solid tissues. PLoS One. 2016;11:e0159961.

39. Kueh AJ, Pal M, Tai L, Liao Y, Smyth GK, Shi W, et al. An update on using CRISPR/Cas9 in the one-cell stage mouse embryo for generating complex mutant alleles. Cell Death Differ. 2017;24:1821–2.

40. Li G, Xie C, Lu S, Nichols RG, Tian Y, Li L, et al. Intermittent fasting promotes white adipose Browning and Decreases obesity by shaping the gut microbiota. Cell Metab. 2017;26:672–685.e674.

41. Frizzell H, Fonseca R, Christo SN, Evrard M, Cruz-Gomez S, Zanluqui NG, et al. Organ-specific isoform selection of fatty acid-binding proteins in tissue-resident lymphocytes. Sci Immunol. 2020;5(46):eaay9283.

42. Vasanthakumar A, Chisanga D, Blume J, Gloury R, Britt K, Henstridge DC, et al. Sex-specific adipose tissue imprinting of regulatory T cells. Nature. 2020;579:581–5.

43. Belkina AC, Ciccolella CO, Anno R, Halpert R, Spidlen J, Snyder-Cappione JE. Automated optimized parameters for T-distributed stochastic neighbor embedding improve visualization and analysis of large datasets. Nat Commun. 2019;10:5415.

44. Becht E, McInnes L, Healy J, Dutertre CA, Kwok IWH, Ng LG, et al. Dimensionality reduction for visualizing single-cell data using UMAP. Nat Biotechnol. 2018;37:38–44.

## SUPPORTING INFORMATION

Additional supporting information may be found in the online version of the article at the publisher's website.